

Virtual Special Issue Gulf of Mexico Modelling – Lessons from the spill

Modeling the tidal and sub-tidal hydrodynamics in a shallow, micro-tidal estuary



Matthew D. Rayson*, Edward S. Gross, Oliver B. Fringer

Bob and Norma Street Environmental Fluid Dynamics Laboratory, Department of Civil and Environmental Engineering, Stanford University, United States

ARTICLE INFO

Article history:

Received 31 August 2014
Received in revised form 4 February 2015
Accepted 9 February 2015
Available online 25 February 2015

Keywords:

Estuaries
Galveston Bay
Unstructured grid
Surface heat flux
SUNTANS

ABSTRACT

The three-dimensional hydrodynamics of Galveston Bay were simulated in two periods of several month duration. The physical setting of Galveston Bay is described by synthesis of long-term observations. Several processes in addition to tidal hydrodynamics and baroclinic circulation processes contribute substantially to the observed variability of currents, water level and salinity. The model was therefore forced with realistic water levels, river discharges, winds, coastal buoyancy currents (due to the Mississippi River plume) and surface heat fluxes. Quantitative metrics were used to evaluate model performance against observations and both spatial and temporal variability in tidal and sub-tidal hydrodynamics were generally well represented by the model. Three different unstructured meshes were tested, a triangular mesh that under-resolved the shipping channel, a triangular mesh that resolved it, and a mixed quadrilateral-triangular grid with approximately equivalent resolution. It is shown that salinity and sub-tidal velocity are better predicted when the important topographic features, such as the shipping channel, are resolved. It was necessary to increase the seabed drag roughness in the mixed quadrilateral-triangular grid simulation to attain similar performance to the equivalent triangular mesh.

© 2015 Elsevier Ltd. All rights reserved.

1. Introduction

Galveston Bay is one of the largest estuaries on the Gulf Coast and is the busiest petrochemical port in the United States. In addition to heavy industrial use, the estuary has a substantial ecological function including coastal habitat for migratory birds, oyster production and a recreational fishing industry (Lester and Gonzalez, 2011). Oil spills are common in the bay. Between 1998 and 2009 there were almost 4000 reported spills with a combined volume of 400,000 gallons (Lester and Gonzalez, 2011). In March 2014, 168,000 gallons of heavy bunker fuel was spilled into the bay in a single incident when a ship and a barge collided. Understanding and accurately predicting the estuarine hydrodynamics is a crucial step towards determining the fate and transport of oil in the system.

Galveston Bay covers an area of 1360 km² and has an average depth of 2–3 m (Fig. 1). The man-made Houston Shipping Channel (HSC) is the primary deep bathymetric feature with a depth of 15 m and average width of 200 m traversing from the main Gulf entrance (Bolivar Roads) to the Buffalo Bayou in the

northern part of the bay. The Trinity River enters the shallow Trinity Bay perpendicular to the axis of the shipping channel. The other side embayments, East and West Bay, are topographically separated by the man-made Texas City Dike and Hanna Reef, a natural oyster reef. Most of the heavy industry is along the western shoreline close to the HSC and near Texas City while most of the oyster reefs and bayous that provide bird habitat are in the side embayments and along the eastern shore.

The geomorphological classification of the bay is a coastal lagoon with a barrier island (Schroeder and Wiseman, 1999). The physical setting (geometry, bathymetry, forcing) of the bay is similar to other estuaries along the Gulf Coast (e.g., Mobile Bay, Alabama and Barataria Bay, Louisiana) yet different from the drowned river type estuaries upon which the majority of estuarine literature is based (e.g., Hansen and Rattray, 1966; Geyer and MacCready, 2014).

The Trinity River contributes about 75% of the total flow into Galveston Bay, and the salinity distribution within the bay is primarily driven by freshwater discharge (Orlando, 1993). During a typical year the wet period is April–June and the average salinity within the bay is 5–10 psu lower than the drier months of Aug–Oct. Despite having an average depth of 3 m, Trinity Bay remains

* Corresponding author.

E-mail address: mrayson@stanford.edu (M.D. Rayson).

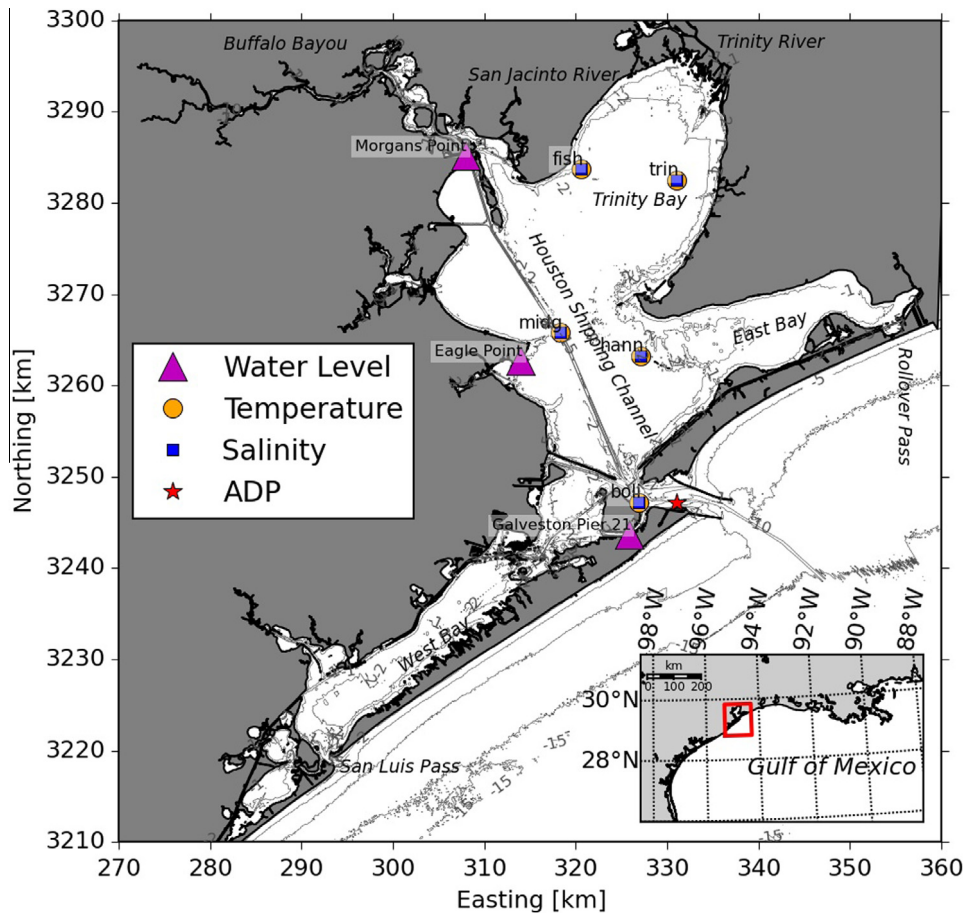


Fig. 1. Bathymetry of Galveston Bay showing the locations of observation sites.

stratified throughout the year. Other than the deeper HSC, this was the only part of the bay that was found to be stratified in the hydrographic observations examined by Orlando (1993). The understanding of salt transport within the bay is that seawater intrudes into the upper reaches of the bay via the HSC and freshwater leaves along the eastern margins (Powell et al., 2003). This general understanding of the bay circulation is based upon limited field observations and coarse resolution hydrodynamic modeling.

The tides in the Gulf of Mexico are classified as micro-tidal and are primarily diurnal. Despite the small amplitude of the tides, topographic features, such as constrictions at the entrances to bays and estuaries, can lead to locally strong tidal currents in excess of 1 m s^{-1} (Schroeder and Wiseman, 1999). Tidal forcing only accounts for a fraction of the total water level variability along the Gulf Coast; Ekman setup due to the east–west component of wind stress as well as seasonal variations in the circulation in the Gulf of Mexico also drive substantial water level fluctuations (Schroeder and Wiseman, 1999; Cox et al., 2002). Cox et al. (2002) improved their water level predictions by including the tidal variability plus a linear regression model relating wind stress to water level.

Previous Galveston Bay hydrodynamic model applications have addressed several issues but little of this work is available in peer-reviewed journals. Berger et al. (1995) developed a 3D finite-element model that was used to evaluate the effect of modifications to the shipping channel on salinity distribution. The 3D model had three vertical layers. Klinck and Hofmann (2002) coupled the model of Berger et al. (1995) to an oyster population model to show that widening the HSC would increase the habitable region within the bay. Matsumoto et al. (2005) developed a

depth-averaged model of the bay to understand the influence of structures such as the Texas City Dike on the residual circulation patterns in the bay. An operational nowcast/forecast model has been developed to provide water level and currents for navigation and also for oil spill response (Schmalz, 2000; Schmalz and Grant, 2000). In this model, the bay and shipping channel were discretized using separate grids to resolve the length scale differences between the shipping channel and the rest of the bay. While the model of Schmalz and Grant (2000) was able to resolve the velocity and water level throughout the bay fairly accurately, it under-represented the salinity stratification observed within the shipping channel. A common weakness in all of these models was that three-dimensional processes, such as vertical shear and baroclinic flow, were either ignored or under-resolved.

The purpose of this paper is to describe Galveston Bay's circulation characteristics and present a new hydrodynamic model capable of resolving the important processes. Modeling oil transport in the embayments bordering the Gulf of Mexico is the motivation for developing this model. Accurately simulating the hydrodynamics that drive oil transport is a multi-scale physics problem in which the full space–time spectrum of variability must be captured. Aspects of Galveston Bay hydrodynamics considered include salinity variability and its relationship to freshwater discharge, tidal dynamics including tidal frequency and the sub-tidal frequency water level and current variability and water temperature variability. Water temperature is often neglected in estuarine models due to the dominance of salinity on the baroclinic pressure gradient, however we include it because it influences the evaporation rate and is important for biological processes such as oyster larval recruitment (e.g., Klinck and Hofmann, 2002). Adequate

vertical resolution of three-dimensional variability is an enhancement of this study over previous modeling efforts.

2. Observations of circulation in Galveston Bay

There have been numerous long-term observational deployments taken within Galveston Bay since 1990. We synthesize these data sets to provide a coherent description of the physical setting of the bay. This section describes physical processes that are important to reproduce with a numerical model. We focus on the physical variability during two time periods with distinctive freshwater forcing regimes, namely March to September 2009, a winter-summer/wet-dry cycle, and 2011, a drought year. These particular periods were chosen for adequate observational data coverage suitable for both analysis and model validation.

2.1. Description of observations

Hydrodynamic measurements of velocity, water level, temperature, and salinity in Galveston Bay have been collected by NOAA as part of the Texas Coastal Ocean Observing Network (TCOON) since 1995. Furthermore, the Texas Water Development Board (TWDB) has measured temperature and salinity within the bay since 1990. The locations of all instruments are shown in Fig. 1 and details of the variables recorded are listed in Table 1. This is the first peer-reviewed study to synthesize these long-term datasets into a description of the physical setting of Galveston Bay.

The Texas Coastal Ocean Observing Network (TCOON), in partnership with the NOAA Integrated Ocean Observing System (IOOS), has measured water level in Galveston Bay since 1995 (<http://tidesandcurrents.noaa.gov/>) (pink triangles in Fig. 1). We analyzed water level from three stations: Galveston Pier 21 (ID: 8771450), Eagle Point (ID: 8771013) and Morgan's Point (ID: 8770613). All data were sampled at 6 min and adjusted to mean sea level prior to analysis. All data analyzed here extended from 1995–2013 except the Freeport station which began collecting data in August 2006.

We obtained velocity profile observations from NOAA PORTS at the main entrance to Galveston (site name: Galveston Bay Entrance Channel LB11; station ID: g06010, red star Fig. 1) extending from 2009 to 2013. The instrument was a downward looking (buoy mounted) Nortek AquaDopp (ADP) current profiler with 3 beams sampling at 6 min intervals (1800 pings per sample). The instrument was mounted 3 m below the surface in 12 m of water and the vertical resolution was 1 m. Bins near the bottom were deemed unsuitable and we therefore retained bins from 4 to 10 m below the surface.

Temperature and salinity have been continuously measured in Galveston Bay by the TWDB at 10 stations since 1990. We used data from five of these stations that had suitable coverage from 2007–2012 (Fig. 1). TWDB used HydroMap Datasonde that were pre-calibrated before each deployment and cross-checked against

Table 1
Information of observation collected in Galveston Bay by different organizations.

Station ID	Station location	Agency	Variable	Depth [m]
g06010	Galveston Entrance Channel	NOAA PORTS	u, v	3.0
8770613	Morgan's Point	NOAA/TCOON	η	–
8771013	Eagle Point	NOAA/TCOON	η	–
8771450	Galveston Pier 21	NOAA/TCOON	η	–
midg	Mid Galveston Bay	TWDB	T, S	2.5
boli	Bolivar Roads	TWDB	T, S	3.0
fish	Fishers Reef	TWDB	T, S	2.0
trin	Trinity Bay	TWDB	T, S	1.5
hann	Hannah Reef	TWDB	T, S	1.5

CTD casts taken both during deployment and retrieval of the instruments. Deployment periods were typically 3–4 months. Instrument depths (below MSL) are listed in Table 1. We applied quality control to ensure that only valid data were used. The first step was to clip values outside of a reasonable range (0–36 psu, 0–40 °C for salinity and temperature, respectively). The second was to apply a despiking algorithm with a sliding filter that calculated the mean and standard deviation over a 3-day window. Values greater than three times the standard deviation from the mean were discarded. The salinity records were particularly susceptible to drift in the last 2–4 weeks of each deployment. To account for instrument drift, we manually inspected the data for discontinuous salinity between deployment periods and removed suspect data from the record. Quality control resulted in gaps in the observation record. To allow model-observation comparison, the model data was temporally interpolated onto the uneven time step of the observation rather than trying to fill in the gaps. Conductivity was also measured at three TCOON/NOAA stations (Galveston Bay Entrance Channel, Eagle Point and Morgan's Point) but we do not include these data owing to the large temporal gaps in each record.

We have organized the description of each of the variables into their tidal and sub-tidal frequency bands using a Godin-type 24–25–24 h low-pass filter (see Thomson and Emery, 2001) to remove the variability at frequencies at and above the tidal band. Gaps in the record were not included in the mean calculations.

Throughout this paper, the physical variables are decomposed as

$$\phi(z, t) = \langle \phi(z) \rangle + \phi_T(z, t),$$

where the angle brackets indicate a tidal-averaging operator and the subscript T indicates the tidal frequency fluctuation. The notation for depth-averaging over the water column is

$$\bar{\phi} = \frac{1}{d + \eta} \int_{-d}^{\eta} \phi dz.$$

where $-d$ is bed elevation and η is free surface elevation.

2.2. Tidal and sub-tidal water level variability

Tidal and low-frequency water levels are roughly the same amplitude in Galveston Bay with a total range of just over 1 m (Fig. 2). 3–10 d period variability in water level, indicated by the

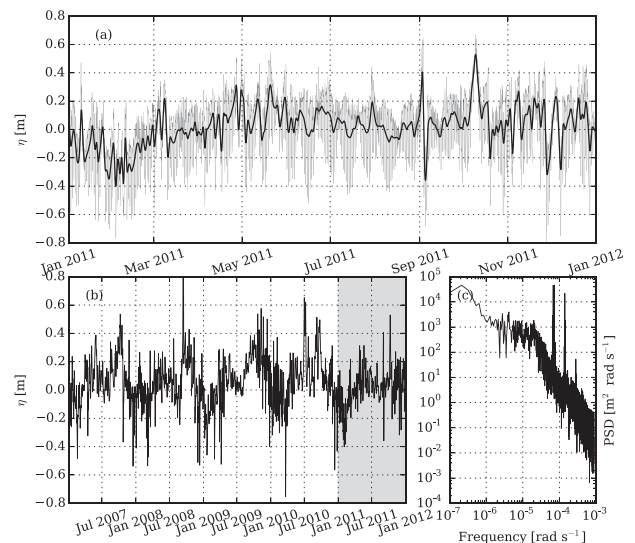


Fig. 2. Sea surface height (relative to mean sea level) variability at Galveston Pier 21 (see Fig. 1) as represented by (a) tidal (η_T , gray) and sub-tidal (η , black) perturbations during 2011, (b) sub-tidal perturbations (η) for the period 2007–2012 and (c) power spectral density of the five-year signal. The gray box in (b) indicates the time span in (a).

black lines in Fig. 2(a), had an amplitude of 0.1–0.4 m and was greatest during the non-summer months (September–June). An annual period signal was evident from longer-term observations (Fig. 2(b)) that had a maximum around October and minimum in February of each year. A power spectrum of the total five-year water level record (Fig. 2(c)) quantifies the variance in each frequency band. Large spectral peaks were present at the annual period ($2 \times 10^{-7} \text{ rad s}^{-1}$) and the diurnal and semi-diurnal frequencies. The weather band ($2 \times 10^{-6} - 2 \times 10^{-5} \text{ rad s}^{-1}$) appeared as a broad, flat region of the spectrum. The broadness of the spectrum reveals that water level, and hence circulation, variability is spread over a wide range of time scales. This is in contrast to tidally-dominated systems in which most of the variance is contained in a small number of tidal constituents.

Tidal harmonic analysis of the observed record collected at Galveston Pier 21 in 2011, revealed the amplitude of individual tidal frequencies. The tidal oscillations in Galveston Bay are mainly diurnal with K_1 and O_1 each having an amplitude of about 0.17 m (Table 2). The semi-diurnal M_2 was the next largest constituent with an amplitude of 0.09 m. The other major constituents were Q_1 , S_2 and N_2 with amplitudes ranging from 0.02–0.04 m. Due to the mixture of constituents, the water level signal was generally diurnal except during diurnal-neap periods when the tidal signal was semi-diurnal. Diurnal-neaps are caused by fortnightly beating of the K_1 and O_1 frequencies and are not to be confused with neap tides caused by the beating of the M_2 and S_2 semi-diurnal constituents, although the overall effect is similar. Harmonic analysis using data from other years revealed inter-annual variations in the tidal range that are consistent with the 18.61 year lunar declination cycle (see Haigh et al., 2011 and references therein). The amplitude of O_1 water level oscillation varied by 30% with a low in 1997 to a peak value in 2006, then decreasing between 2006–2012 consistent with a cyclic modulation pattern. Less than 50% of the total variance of the water level signal was accounted for by the tidal frequency band indicating that a significant portion of the energy is sub-tidal.

Observations from three stations located along the shipping channel (Galveston Entrance, Eagle Point and Morgan's Point) revealed the spatial variability of the tides along the main axis of the bay. There was a general decrease in the amplitude of the three major constituents (K_1 , O_1 and M_2) from the Gulf to the upper reaches (Table 2). The amplitude of the diurnal constituents, K_1 and O_1 , decreased by 20% from the entrance to Eagle Point, and M_2 amplitude decreased by 75% between the two stations. This decrease in amplitude indicates damping of the M_2 tidal wave as it propagates into the bay. The decrease in amplitude of the diurnal constituents between Eagle Point and Morgan's Point was negligible, while there was an increase in the amplitude of the M_2 constituent between the two sites from 0.03 to 0.05 m. The phase lag of the diurnal and semi-diurnal constituents was 4 h from the entrance to Eagle Point and 5–6 h from the entrance to Morgan's Point. The amplification of the M_2 constituent and small phase lag between Eagle Point and Morgan's Point suggest standing wave behavior caused by reflections of tides at the shoreline of Galveston Bay near Morgan's Point. These results are approximately in agreement with the tidal analysis performed by Hess et al. (2004) who used tidal predictions for correcting bathymetric survey data within Galveston Bay.

Table 2

Tidal harmonic amplitude and phase for the year 2010 at three stations within Galveston Bay.

Station	K_1 amp [m]	K_1 phase [°]	O_1 amp [m]	O_1 phase [°]	M_2 amp [m]	M_2 phase [°]
Galveston Entrance	0.14	160	0.14	92	0.13	284
Eagle Point	0.11	228	0.11	150	0.03	23
Morgan's Point	0.12	243	0.12	162	0.05	70

Table 3

Water level and depth-averaged current tidal amplitude and phase near the entrance to Galveston Bay during 2011.

Frequency	η_{amp} [m]	\bar{u}_{maj} [m s ⁻¹]	\bar{u}_{min}	$\theta_{ellipse}$	η_{phs}	\bar{u}_{phs}
M_2	0.090	0.265	-0.020	7.577	57.082	-111.613
S_2	0.026	0.065	-0.005	9.707	111.879	-65.782
N_2	0.024	0.054	-0.004	13.617	144.041	-30.762
K_2	0.005	0.058	0.013	14.220	298.649	53.221
K_1	0.130	0.369	0.030	9.930	180.336	-36.118
O_1	0.124	0.342	0.028	9.654	220.551	1.436
P_1	0.035	0.100	0.002	18.217	267.335	77.243
Q_1	0.023	0.049	0.007	13.443	307.685	93.231
M_4	0.005	0.032	-0.006	-1.176	321.739	74.237
MK_3	0.000	0.021	-0.010	-10.128	153.697	150.631
MN_4	0.002	0.014	-0.002	176.334	26.880	-3.430
NU_2	0.006	0.025	0.000	6.668	246.289	82.976

2.3. Currents through the main entrance

The depth-averaged velocity measured at Galveston Entrance (ID: g06010) had a peak of 0.8–0.9 m s⁻¹. The larger fluctuations were in the tidal band while peak velocities in the sub-tidal bands were around 0.2–0.3 m s⁻¹. This is in contrast to the water level where fluctuations at the tidal and sub-tidal frequencies were on the same order.

2.3.1. Tidal frequency currents

Depth-averaged tidal frequency currents at the entrance ADP were up to 0.9 m s⁻¹. Tidal ellipse parameters for eight dominant constituents and four nonlinear super-harmonics are shown in Table 3. The K_1 and O_1 constituents were dominant; the magnitude of the semi-major axis of the tidal ellipses for these constituents was 0.37 and 0.34 m s⁻¹, respectively. The M_2 amplitude was 0.27 m s⁻¹. The other important diurnal (J_1 , Q_1 , S_1 and M_1) and semi-diurnal (S_2 , N_2 , L_2 and K_2) constituents each had an amplitude ranging between 0.02 m s⁻¹ and 0.07 m s⁻¹. The magnitude of the semi-major axis of the tidal ellipses of nonlinear harmonics were generally an order of magnitude lower than the forcing frequencies (0.01–0.03 m s⁻¹).

2.3.2. Sub-tidal currents

The depth-averaged, sub-tidal currents measured at the entrance ADP had a maximum amplitude of 0.30 m s⁻¹ and a period of 3–10 days consistent with the weather band (Fig. 3(a)). The outgoing phase (positive \bar{u}) of the oscillation was usually stronger indicating net low-frequency outflow at this site. There was a distinct period during the summer months (Jun–Aug) when the low-frequency velocity fluctuations were significantly diminished, averaging less than 0.05 m s⁻¹.

An analysis of cross-correlation of east–west wind velocity at the Galveston met station with water level at Galveston Pier 21 indicated significant correlation ($r^2 = -0.5$) with zero lag (not shown). The negative correlation arises from Ekman dynamics in which westward winds (negative stress) drive the water level up and eastward winds (positive stress) drives the water level down. Cross-correlation between the low-frequency water level and barotropic currents near the entrance revealed a significant relationship ($r^2 = 0.5$) with a lag time of roughly 24 h (water level lagged the currents).

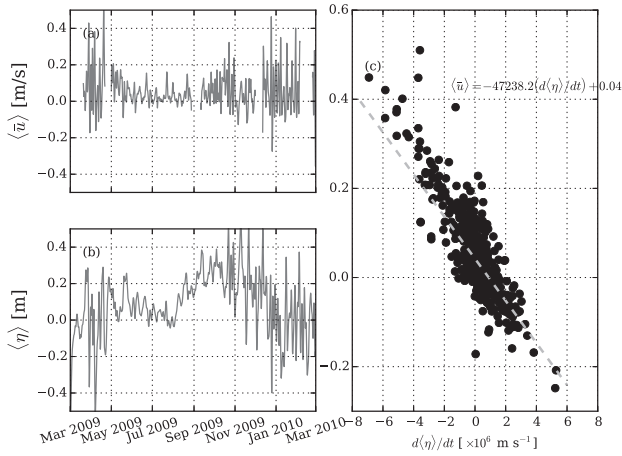


Fig. 3. Time-series of low frequency, depth-averaged velocity through the main entrance to Galveston Bay (a) with low-frequency water level (b) over the same period in 2011. (c) Scatter plot highlighting the linear relationship between the time-rate of change of sub-tidal water level and barotropic velocity.

Fig. 3(c) shows an approximately linear relationship between $\langle \bar{u} \rangle$ and $d\langle \eta \rangle/dt$ suggesting that the sub-tidal volume flux into the bay can be modeled with

$$\langle Q \rangle \sim A_{bay} \frac{d\langle \eta \rangle}{dt} \quad (1)$$

where A_{bay} is the surface area of the bay, $\langle Q \rangle \approx \langle \bar{u} \rangle A_{entrance}$, and $A_{entrance}$ is the cross-sectional area at the entrance. Assuming that the sub-tidal water level fluctuations are sinusoid-like, a quarter period lag is expected between water level and volume flux based on (1). The roughly 24 h lag observed here is therefore consistent with a 3–7 d oscillation.

2.4. Salinity

Observations from three TWDB stations between 2007 and 2012 (Fig. 4(a)) revealed the time and spatial scales of salinity variability within Galveston Bay. The sub-tidal salinity varied from 15–35 psu at the *boli* (main entrance) site to 0–30 psu at the *trin* (Trinity Bay) site (Fig. 4(a)). The mean salinity over the five year period was 12 and 24 psu at *trin* and *boli*, respectively. Salinity differences between these stations persisted throughout the record.

Temporal salinity variability in Galveston Bay is mainly driven by variations in discharge from the Trinity River (Orlando, 1993). There was a distinct seasonal discharge pattern with the highest average discharge in Feb–Mar ($Q = 300\text{--}375 \text{ m}^3 \text{ s}^{-1}$) and the lowest discharge in Aug–Sep with a mean of around $100 \text{ m}^3 \text{ s}^{-1}$ (Fig. 4(b)). Peak discharge events ($>1000 \text{ m}^3 \text{ s}^{-1}$) were intermittent although they had the greatest effect on observed salinity distribution. For example, salinity at all three stations dropped significantly after a flooding event in May 2009. Salinity in Trinity Bay dropped to zero following each large flooding event. During dry periods (i.e., 2011), discharge was three orders of magnitude lower and the salinity gradually increased over a period of several months. As a result the longitudinal gradient decreased roughly ten-fold during dry periods. Salinity near the entrance (*boli*) was far more variable than further upstream at periods of weeks to months. This suggests that other processes are responsible for variability at the entrance, which we will investigate using the numerical model in Section 4.2.

2.5. Water temperature

Long-term temperature observations within the bay revealed significant peaks at the annual and diurnal frequencies. The annual

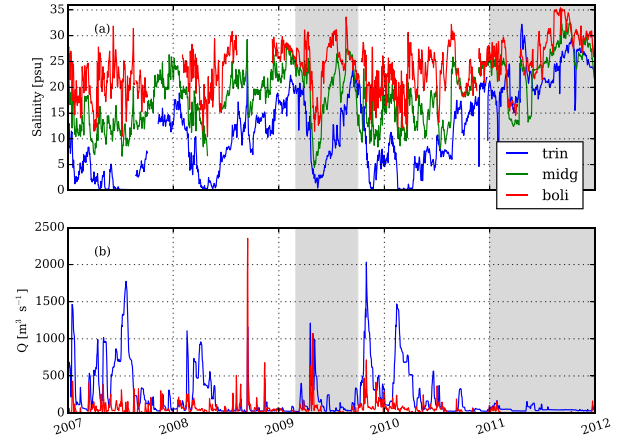


Fig. 4. (a) Five year time series of salinity observations at three stations in the lower (*boli*), mid (*midg*) and upper (*trin*) reaches of the bay. (b) Total discharge from the Trinity River (blue) and the Lake Houston overflow (red). The gray boxes indicate the two model validation time periods. (For interpretation of the references to color in this figure legend, the reader is referred to the web version of this article.)

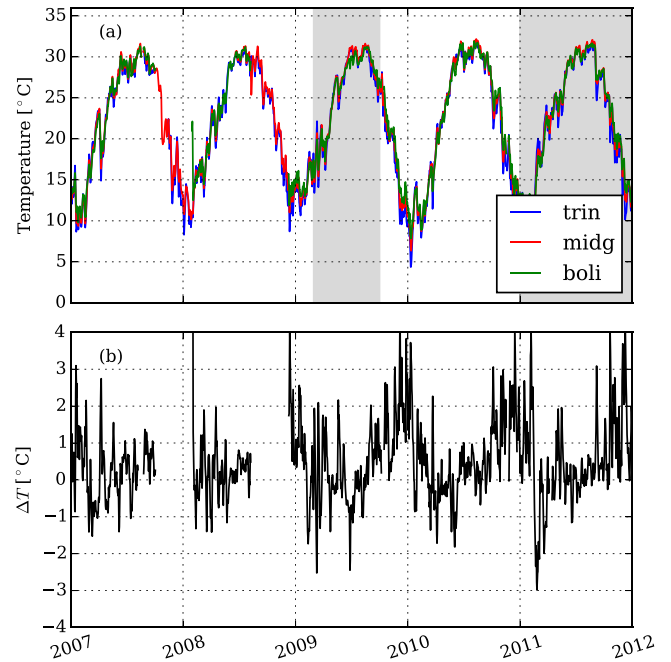


Fig. 5. (a) Five year time series of water temperature observations at three stations in the lower (*boli*), mid (*midg*) and upper (*trin*) reaches of the bay. (b) Temperature difference between *boli* and *trin* stations.

cycle, shown in Fig. 5(a), had a mean of $20 \text{ }^\circ\text{C}$ and an amplitude of $10 \text{ }^\circ\text{C}$ with a minimum in January and maximum in August. The daily temperature cycle amplitude were time-dependent, but on average, the largest daily RMS was during the summer months when solar radiation was largest. Temporal oscillations with periods consistent with the weather band (3–10 d) were also superimposed on the annual temperature cycle.

A spatial temperature difference (ΔT) of up to $4 \text{ }^\circ\text{C}$ intermittently developed between the *boli* and the *trin* stations, where $\Delta T = T_{boli} - T_{trin}$ (Fig. 5(b)). The water temperature at the entrance (*boli*) was generally warmer than Trinity Bay (*trin*), particularly during the cooling phase of the annual cycle e.g., July 2009–Feb 2010, indicating that the shallow regions of the bay were cooling (but not heating) more rapidly than the deeper parts.

The observations indicate that heating and cooling in the bay is spatially variable. Spatial variations in water temperature during

the cooling period will create a density gradient, although this is small compared to the gradient induced by salinity. The influence of water temperature on estuarine circulation will therefore only be important during extremely dry periods when salinity gradients are weak. Water temperature does, however, influence processes other than estuarine circulation, for example the weathering and evaporation of oil (see [Reed et al., 1999](#)).

3. Numerical model setup methodology

We employ the hydrostatic version of the SUNTANS model ([Fringer et al., 2006](#)) to simulate the hydrodynamics of Galveston Bay. The model solves the Reynolds-averaged Navier–Stokes equations with the Boussinesq and hydrostatic approximations,

$$\frac{\partial u}{\partial t} + \nabla \cdot (\mathbf{u}u) - f v = -g \frac{\partial}{\partial x} (\eta + r) + \nabla_H \cdot (v_H \nabla u) + \frac{\partial}{\partial z} \left(v_v \frac{\partial u}{\partial z} \right), \quad (2)$$

$$\frac{\partial v}{\partial t} + \nabla \cdot (\mathbf{u}v) + f u = -g \frac{\partial}{\partial y} (\eta + r) + \nabla_H \cdot (v_H \nabla v) + \frac{\partial}{\partial z} \left(v_v \frac{\partial v}{\partial z} \right), \quad (3)$$

where $\mathbf{u} = (u, v, w)$ are the eastward, northward and vertical velocity components, respectively, f is the Coriolis frequency, and v_H and v_v are the horizontal and vertical eddy viscosity. The free surface elevation is η and r is the baroclinic pressure head given by

$$r = \frac{1}{\rho_0} \int_z^\eta \rho dz, \quad (4)$$

where ρ_0 is the reference density (1000 kg m^{-3}), and ρ is a perturbation density.

The continuity equation has the form

$$\nabla \cdot \mathbf{u} = 0, \quad (5)$$

and the free surface is updated by solving the depth-integrated version of (5)

$$\frac{\partial \eta}{\partial t} + \frac{\partial}{\partial x} \left(\int_{-d}^\eta u dz \right) + \frac{\partial}{\partial y} \left(\int_{-d}^\eta v dz \right) = 0. \quad (6)$$

The tracer (temperature and salinity) transport equations are described in Section 3.1. The model equations are discretized using an unstructured horizontal grid (both triangles and quadrilaterals) with fixed vertical z -layer coordinates.

3.1. Surface heat and salt flux parameterizations

We added surface heat and salt source terms to the SUNTANS model to simulate the effects of atmospheric heating and cooling plus evaporation and precipitation.

Following [Wood \(2008\)](#), the transport equation for temperature T is

$$\frac{\partial T}{\partial t} + \nabla \cdot (\mathbf{u}T) = \frac{\partial}{\partial z} \left(K_T \frac{\partial T}{\partial z} \right) + \frac{\partial Q_{sw}}{\partial z} \quad (7)$$

where \mathbf{u} is the velocity vector, K_T is the vertical eddy diffusivity, and Q_{sw} is the penetrative shortwave radiation flux, in $^\circ\text{C m s}^{-1}$. The surface boundary condition for Eq. (7) implies a heat flux at the free surface $z = \eta$, of the form

$$K_T \frac{\partial T}{\partial z} \Big|_{z=\eta} = Q_s, \quad (8)$$

where Q_s is the surface temperature flux, in $^\circ\text{C m s}^{-1}$. At the bottom boundary, where $z = -d(x, y)$, there is no heat flux, giving

$$K_T \frac{\partial T}{\partial z} \Big|_{z=-d} = 0. \quad (9)$$

The surface temperature source term, Q_s , is composed of upward and downward longwave radiation, $H_{lw,u}$ and $H_{lw,d}$, respectively, latent or evaporative heat flux H_L , and sensible or conductive heat flux H_S , such that

$$Q_s = \frac{H_{lw,u} + H_{lw,d} + H_L + H_S}{\rho c_p}, \quad (10)$$

where c_p is the specific heat of seawater ($=4186 \text{ J kg}^{-1} \text{ K}^{-1}$). All units for heat flux variables are in W m^{-2} and negative values imply upward flux (heat loss from the surface) and positive values imply downward flux, or flux of heat into the water column. Details of the parameterizations for the shortwave radiation Q_{sw} and each term in Eq. (10) are provided in [Appendix A](#), while the numerical implementation of the temperature and salinity source terms is outlined in [Appendix B](#).

3.1.1. Salt transport

The equation for salt transport is very similar to the temperature Eq. (7) without the penetrative shortwave radiation flux term on the RHS, and is given by,

$$\frac{\partial S}{\partial t} + \nabla \cdot (\mathbf{u}S) = \frac{\partial}{\partial z} \left(K_S \frac{\partial S}{\partial z} \right) \quad (11)$$

We modeled the process of evaporation and precipitation using salt fluxes rather than volume fluxes. Representing evaporation and precipitation as a surface concentration flux, rather than a mass flux as it is in reality, is a common technique used amongst a similar class of coastal ocean models e.g., ROMS ([Haidvogel et al., 2008](#)) and the General Estuarine Transport Model (GETM; [Burchard et al., 2004](#)). The surface boundary condition for the salinity equation is given by

$$K_T \frac{\partial S}{\partial z} \Big|_{z=\eta} = EP \times S_{k_{top}}, \quad (12)$$

where $S_{k_{top}}$ is the salinity in the top cell and the difference between the evaporation and precipitation rates (in m s^{-1}) is given by

$$EP = \frac{1}{\rho_{fresh}} \left(\frac{H_L}{\rho_0 L_v} - \text{rain} \right),$$

where L_v is the latent heat of vaporization for water ($2.26 \times 10^6 \text{ J kg}^{-1}$), ρ_{fresh} is the density of fresh water (1000 kg m^{-3}), and rain is the rainfall rate (in $\text{kg m}^{-2} \text{ s}^{-1}$).

Tracer advection was computed using a higher-order total variance diminishing scheme, which was shown by [Chua and Fringer \(2011\)](#) to reproduce the salinity dynamics in San Francisco Bay.

3.2. Model parameters and numerical schemes

The surface, $z = \eta(x, y, t)$, and seabed, $z = -d(x, y)$, boundary conditions of the horizontal momentum Eqs. (2) and (3) are

$$v_v \frac{\partial \mathbf{u}}{\partial z} \Big|_{z=\eta} = \frac{\vec{\tau}_s}{\rho_0} \quad (13)$$

$$v_v \frac{\partial \mathbf{u}}{\partial z} \Big|_{z=-d} = \frac{\vec{\tau}_b}{\rho_0} \quad (14)$$

where $\vec{\tau}_s = (\tau_{x,s}, \tau_{y,s})$ and $\vec{\tau}_b = (\tau_{x,b}, \tau_{y,b})$ are the surface and seabed stress components, respectively. The surface stress is parameterized by

$$\vec{\tau}_s = C_{da} \rho_a |\mathbf{U}_a| (\mathbf{U}_a - \mathbf{u}|_{z=\eta}) \quad (15)$$

where ρ_a is the density of air (1.2 kg m^{-3}), \mathbf{U}_a is the horizontal wind velocity vector, and C_{da} is the empirical surface drag coefficient. A

quadratic drag formulation was also used to define the seabed stress

$$\vec{\tau}_b = -\rho_0 C_d |\mathbf{u}|_{z=-d} |\mathbf{u}|_{z=-d} \quad (16)$$

The bed drag coefficient is parameterized using a log-law formulation

$$C_d = \left[\frac{1}{\kappa} \ln \left(\frac{z}{z_0} \right) \right]^{-2} \quad (17)$$

where κ is von Kármán's constant (0.41), z is the height above the bed of the center of the bottom grid cell ($0.5\Delta z$), and z_0 is a bottom roughness coefficient. Surface drag coefficient was either calculated using the COARE 3.0 algorithm (Fairall and Bradley, 2003), which is wind speed dependent, otherwise we set it constant ($C_{da} = 1.10 \times 10^{-3}$).

The horizontal eddy viscosity was constant ($\nu_H = 1.0 \text{ m}^2 \text{ s}^{-1}$) and the vertical eddy viscosity was computed by the Mellor and Yamada (1982) (MY2.5) turbulence closure scheme. Advection of momentum was computed by a first-order upwind scheme. A linear equation of state was used to compute the density perturbation, ρ , as a function of both salinity and temperature

$$\frac{\rho(s, T)}{\rho_0} = \beta(s - s_0) - \alpha(T - T_0) \quad (18)$$

where $s_0 = 12.5$ psu and $T_0 = 20.0$ °C are reference values for temperature and salinity, β is the haline contraction coefficient ($7.52 \times 10^{-4} \text{ psu}^{-1} \text{ kg m}^{-3}$), and α is the thermal expansion coefficient ($2.2 \times 10^{-4} \text{ °C}^{-1} \text{ kg m}^{-3}$).

3.3. Grid and bathymetry

A major challenge in modeling a geometrically complex region like Galveston Bay is resolving the bathymetric features that are pertinent to the bulk circulation of the bay. Important features, like the Houston Shipping Channel, have length scales ranging from 10 to 100 m while the estuarine length scale is roughly 100 km.

For this study we developed three different unstructured grids capable of resolving the important topographic/geometric properties of Galveston Bay, while still having few enough grid points to be run for months to years on a modest number of processors (32–64). The first grid consisted of 21,484 horizontal grid cells and had a horizontal grid resolution (distance between grid cell centers) ranging from 2000 m at the open boundary down to 400 m within the bay (Fig. 6(a) and (b)). We will refer to this grid as the *coarse triangular grid* or just the *coarse grid* throughout this paper. A finer resolution triangular grid was developed to test the sensitivity of the resolution on model performance (Fig. 6(c)). The median horizontal spacing of this grid (the *fine triangular grid* or just the *fine grid*) was 95 m and the resolution was focused on the Houston Shipping Channel and the entrance of Galveston Bay. The *fine triangular grid* consisted of 59,818 horizontal cells.

Triangular unstructured meshes can induce higher numerical diffusion compared to an equivalent rectangular grid (Holleman et al., 2013, see). Furthermore, errors in the calculation of the horizontal divergence on staggered Arakawa C-grids cause grid-scale numerical noise that projects itself onto the vertical velocity field (Wolfram et al., 2013). To minimize these issues we constructed a mixed quadrilateral-triangular grid with quadrilaterals employed in key high velocity regions (Fig. 6(d)) using the *Janet* grid generation package developed by Smile Consult (www.smileconsult.de). Roughly uniform resolution quadrilaterals ($\Delta x = 100$ m) were paved in the Houston Shipping Channel and through the entrance of Galveston Bay. The rest of the grid consisted of triangles. The total number of horizontal cells was 57,305, with 20 vertical layers resulting in 478,984 total active 3D cells.

The model bathymetry was specified using a Galveston Bay 1/3 arc second (10 m) digital elevation model (DEM) (Taylor, 2008). This DEM was generated using bathymetry data from various sources (soundings, LIDAR, side-scan sonar) the most recent of which was collected in 2008. It should be noted that the bathymetry of the bay is constantly evolving, particularly in the wake of major hurricanes.

3.4. Open boundary and initial conditions

3.4.1. Tides and water level

The tidal frequency water level and velocity data were specified along the open boundaries with a combination of coastal tide gauge data and tidal constituent information from a Gulf of Mexico regional tidal model (Egbert and Erofeeva, 2002). The motivation for using the two data sets was to capture the full temporal spectrum (tidal and sub-tidal frequencies) using the gauged data while also representing the spatial variability of the tides.

To blend the tide gauge and tidal model data, first, water level and velocity amplitude ($A_{mod,m}(x, y)$) and phase ($\phi_{mod,m}(x, y)$) from the Oregon State University 1/45th degree resolution Gulf of Mexico regional tidal model were interpolated onto the boundary cells for each of the eight resolved tidal constituents: $M_2, S_2, N_2, K_2, K_1, O_1, P_1, Q_1$. Next, we performed a least-squares harmonic fit of the tide gauge data for the model period (6–12 months) using the same eight tidal constituents to give $A_{obs,m}$ and $\phi_{obs,m}$, the observed amplitude and phase, respectively. The subscript m represents the tidal constituent number. The tidal model predicted amplitude at each location was multiplied by the ratio of observed to predicted amplitude at the gauge (x_g, y_g) i.e.,

$$A_m(x, y) = \frac{A_{obs,m}}{A_{mod,m}(x_g, y_g)} A_{mod,m}(x, y) \quad (19)$$

Similarly, the difference between the observed phase and the modeled phase at the tide gauge location was applied as a correction

$$\phi_m(x, y) = \phi_{mod,m}(x, y) + [\phi_{obs,m} - \phi_{mod,m}(x_g, y_g)] \quad (20)$$

The same correction was applied to all boundary cells for both water level and velocity. Using this technique, we resolved the spatial variability predicted by the tidal model while preserving the observed phase and amplitude modulation recorded at the tide gauge.

Finally the residual signal was added to all open boundary points. This signal contained tidal constituents not included in the tidal model as well as the low frequency (sub-tidal) component of the water level spectrum (e.g., Fig. 2).

3.4.2. Freshwater discharge

Freshwater inputs were specified using output from a coastal hydrology model for the Trinity–San Jacinto estuarine region (Schoenbaechler and Guthrie, 2012). This model included gauged freshwater discharge contributions, agricultural diversion and return flows, and estimated flows from ungauged sections. The total freshwater contribution from ungauged watersheds was significant, particularly during dry periods. Ungauged flow into the Trinity River watershed accounted for >50% of total discharge during low flow conditions but <5% during high flow.

3.4.3. Texas–Louisiana shelf regional model coupling

The salinity along the Texas–Louisiana shelf is heavily influenced by the Mississippi and Atchafalaya River outflows, with values in the Gulf bordering Galveston Bay varying between 20 and 35 psu (Marta-Almeida et al., 2013). To represent this variability we coupled the SUNTANS open boundaries with a shelf-scale Regional Ocean Modeling System (ROMS; Haidvogel et al., 2008)

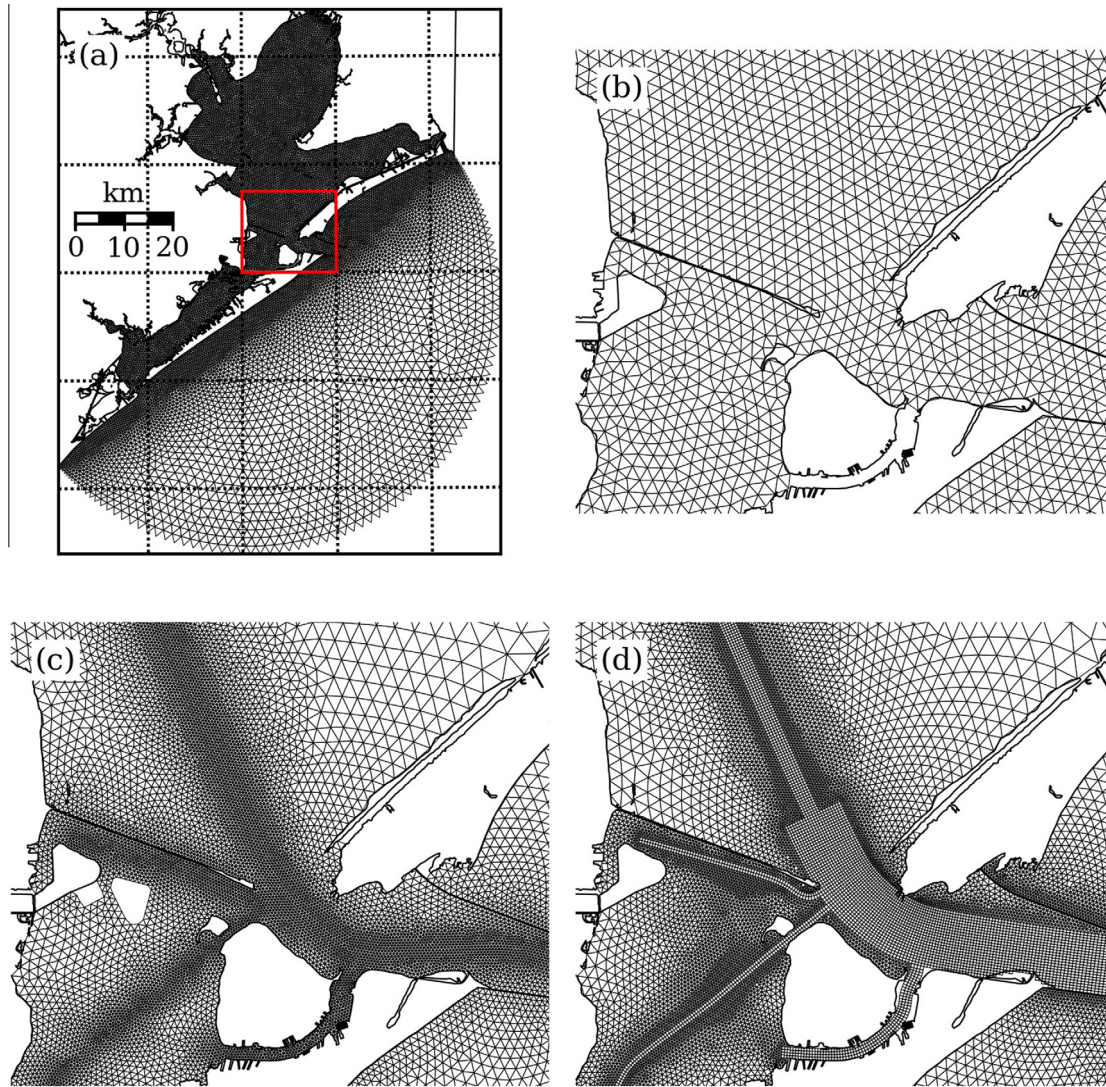


Fig. 6. (a) The extent of the coarse SUNTANS grid with the red square indicating the region detailed in (b)–(d). Zoom in of the (b) coarse grid, (c) the fine triangular grid, and (d) the mixed quad-tri grid near the entrance of the bay. (For interpretation of the references to color in this figure legend, the reader is referred to the web version of this article.)

model that reproduced the regional salinity characteristics (Hetland and DiMarco, 2012; Marta-Almeida et al., 2013; Zhang et al., 2012).

Temperature and salinity boundary conditions within the Gulf were obtained from the shelf-scale ROMS model of Zhang et al., 2012. The data from the ROMS model was first spatially interpolated onto the SUNTANS open boundary cells using inverse distance interpolation and then interpolated vertically from the ROMS to SUNTANS cell centers. ROMS 4-h output was interpolated in time to coincide with the 1-h tidal forcing interval.

Initial temperature and salinity conditions were also specified using ROMS predictions. The ROMS grid coarsely resolved Galveston Bay and accounted for Trinity River inflow. Because there was no tidal forcing in the ROMS model the initial temperature and salinity fields were approximate. Two weeks of spin up time were required for these fields to roughly achieve equilibrium with the tidal forcing.

3.5. Atmospheric forcing

The atmospheric forcing data was specified using the North American Regional Reanalysis (NARR) data set (Mesinger et al.,

2006). This model hindcasts the atmospheric state and outputs the data on a ~ 40 km grid at a 3 h interval. Atmospheric variables required by the heat flux parameterization (described below) were wind velocity at 10 m, mean sea-level air pressure, air temperature, relative humidity, cloud cover and precipitation. Net long-wave and shortwave radiation were derived in the model (see Appendix). All variables were input into SUNTANS on the NARR space-time grid and interpolated internally within the model. Spatial interpolation of the variables was performed using ordinary kriging (optimal interpolation) (see e.g., Cressie, 1990). A spherical model was used to model the covariance between points and we used a wide spatial range parameter (50 km) to ensure smoothness of the interpolated fields. Quadratic interpolation was used to interpolate onto the model time step.

3.6. Model evaluation metrics

Quantitative skill assessment is necessary to evaluate the performance of our numerical model and its usefulness to other applications. Similar to other hydrodynamic model validations in estuaries (e.g., Wang et al., 2011) and the coastal ocean (e.g., Hetland and DiMarco, 2012), we used the following metrics to

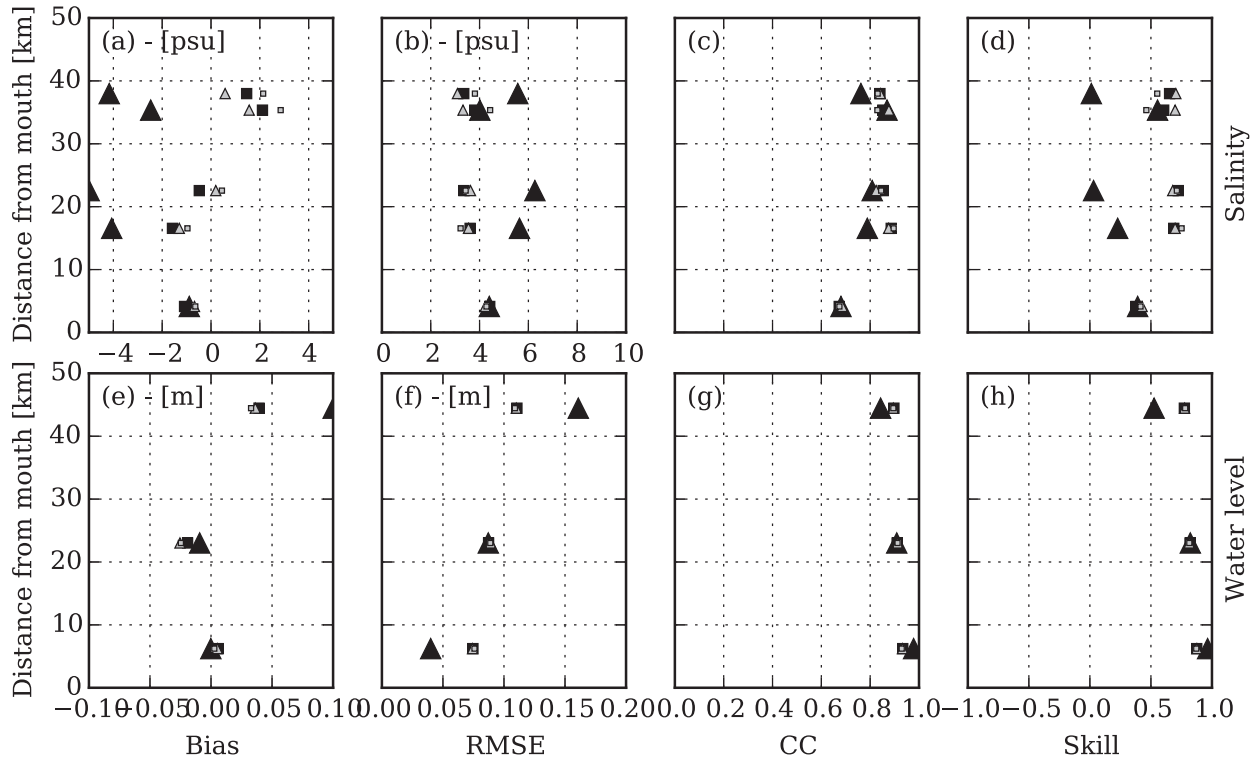


Fig. 7. Model inter-comparison statistics for the 2009 model period. Each row corresponds to a different variable: salinity and water level, respectively; each column corresponds to a different model evaluation statistic: bias, RMSE, CC and skill score. The large black triangles represent the *coarse triangular* grid results, the small gray triangles represent the *fine triangular* grid, gray squares represent the *mixed quad-tri* grid with $z_0 = 2 \times 10^{-5}$ m, and the black squares represent the *mixed quad-tri* grid with $z_0 = 2 \times 10^{-4}$ m.

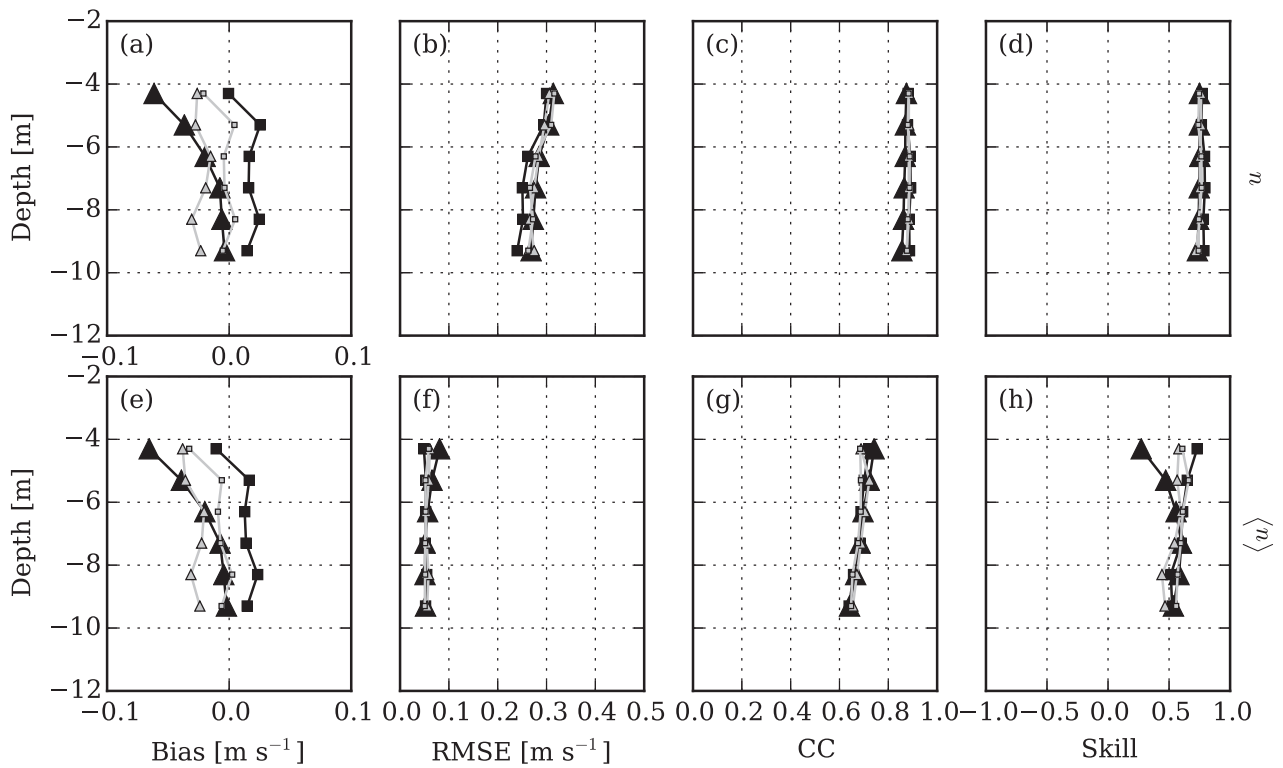


Fig. 8. Model velocity inter-comparison statistics for the 2009 model period as a function of depth. Each row corresponds to a different variable: raw and sub-tidal eastward velocity, respectively; each column corresponds to a different model evaluation statistic: bias, RMSE, CC and skill score. The large black triangles represent the coarse grid results, the small gray triangles represent the *fine triangular* mesh, gray squares represent the *mixed quad-tri* grid with $z_0 = 2 \times 10^{-5}$ m, and the black squares represent the *mixed quad-tri* grid with $z_0 = 2 \times 10^{-4}$ m.

quantitatively evaluate the ability of SUNTANS to reproduce the observed physical processes in Galveston Bay: the model skill score (Murphy, 1988)

$$skill = 1 - \frac{\sum [X_{obs} - X_{mod}]^2}{\sum [X_{obs} - \bar{X}_{obs}]^2}, \quad (21)$$

the root mean squared error (RMSE)

$$RMSE = \sqrt{\frac{1}{N} \sum [X_{obs} - X_{mod}]^2}, \quad (22)$$

the correlation coefficient (CC)

$$CC = \frac{1}{N} \frac{\sum (X_{obs} - \bar{X}_{obs})(X_{mod} - \bar{X}_{mod})}{\sigma_{obs}\sigma_{mod}}, \quad (23)$$

and the bias (mean error)

$$Bias = \frac{1}{N} \sum (X_{mod} - X_{obs}), \quad (24)$$

where X_{obs} and X_{mod} are the discrete observation and model value of a given variable, respectively, \bar{X}_{obs} and \bar{X}_{mod} represent the associated means, σ_{obs} and σ_{mod} represent the standard deviation and N represents the number of observations.

3.7. SUNTANS scenarios

We simulated two time periods with distinctive freshwater forcing regimes: (1) Mar–Sep 2009, a winter-summer/wet-dry cycle, and (2) Jan–Oct 2011, a drought year. These periods were chosen so that the full spectrum of variability would be simulated by the model including periods of low and high river discharge, spring and neap tidal forcing, as well as summer and winter atmospheric conditions. The other motivation for choosing these two periods was that sufficient observations were available to evaluate

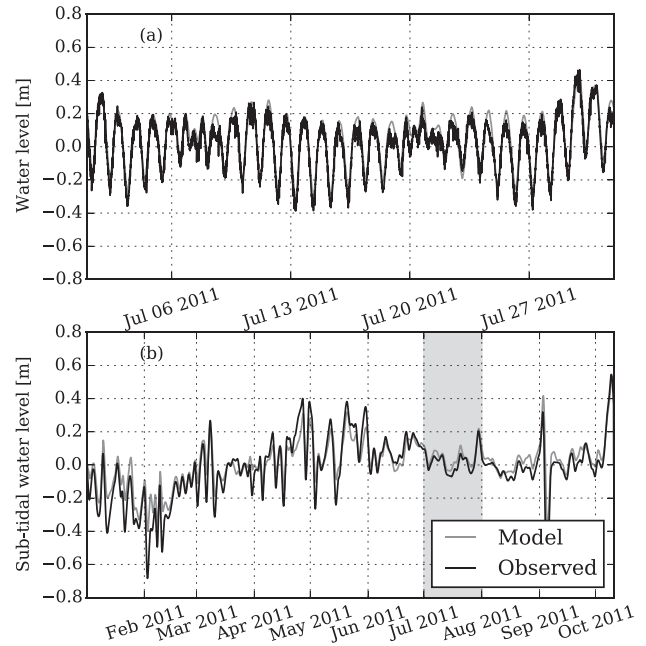


Fig. 10. Model comparison of (a) raw water level for July 2011 and (b) the sub-tidal component for 2011 at Morgan's Point. The gray region in (b) indicates the time period shown in (a).

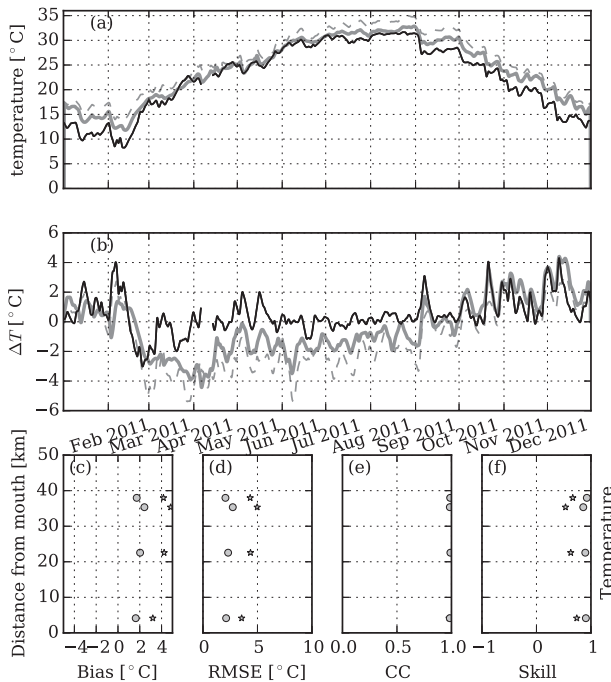


Fig. 9. Model comparison of 2011 water temperature at station boli. (a) Sub-tidal frequency temperature from the observation (black), SUNTANS result with COARE3.0 heat flux algorithm (solid gray), and SUNTANS result with constant heat flux coefficients (dashed gray). (b) The temperature difference between boli and trin stations. (c) Bias, (d) RMSE, (e) correlation coefficient, and (f) model skill of the raw temperature over the 2011 period from the COARE3.0 (circle) and constant coefficient (star) scenarios.

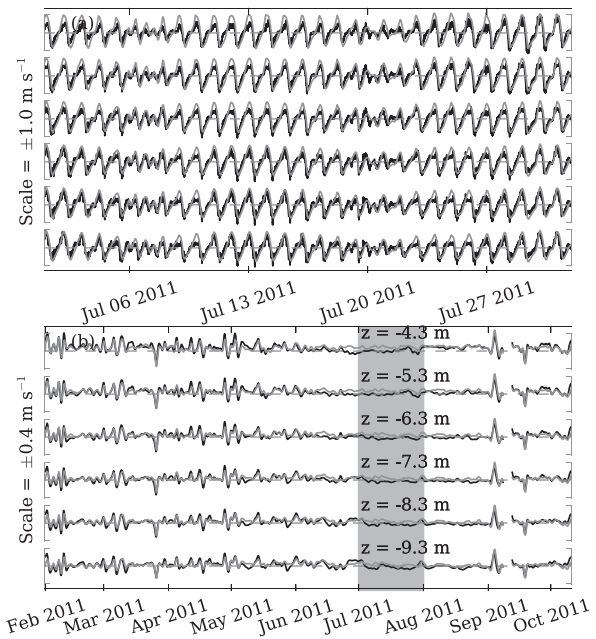


Fig. 11. Model and observed (a) raw and (b) sub-tidal frequency eastward (u) water velocity for each ADP depth bin. The gray region in (b) indicates the time period shown in (a). Depths are meters below mean sea level.

performance. We tested the sensitivity of modeled water temperature to the heat flux parameterization (see Appendix) as well as the influence of bed roughness (drag).

A numerical time step, Δt , of 30 s for the coarse grid and 2 s for the two finer grids was required to ensure model stability. The run time for a six month simulation period was 14 h on 48 CPUs for the coarse grid and roughly 240 h using 62 CPUs for the finer grids. The order of magnitude increase in run times arose from the increase in number of grid points by a factor of two along with a decrease in the time-step size by a factor of 15.

4. Model results

4.1. Model sensitivity

4.1.1. Grid sensitivity

Salinity and water level validation statistics for the three different model grid simulations (*coarse triangular*, *fine triangular*, *mixed quad-tri*) from March–October 2009 are shown in Fig. 7. Overall, all four model performance metrics for salinity (Fig. 7(a)–(d)) from both the *fine triangular* mesh and the *mixed quad-tri* mesh simulations were better than the *coarse triangular* mesh simulation. There was a fresh bias of 2–5 psu at all of the upstream stations in the *coarse triangular* mesh simulation that was corrected in the *fine triangular* and *mixed quad-tri* mesh simulations (Fig. 7(a)). The fine mesh model skill scores for salinity (Fig. 7(d)) (0.5–0.7) were higher (0.5–0.7) than the scores for the *coarse triangular* mesh run (0.0–0.5). The salinity bias at the upstream stations was lower for the *fine triangular* mesh simulation (1 psu) than the *mixed quad-tri* simulation (3 psu). Overall, the *fine triangular* mesh performed the best using the same bed roughness

($z_0 = 2 \times 10^{-5}$ m) for all three grids. We will report the influence of bed roughness in the next section.

Predictions of water level were also improved by increasing the grid resolution with the most notable difference at the furthest upstream station (Morgan's Point; Fig. 7(e)–(h)). The bias in the water level at Morgan's Point was 0.1 m for the *coarse triangular* mesh and 0.04 m for both fine meshes (Fig. 7(e)). The water level RMSE for the fine mesh simulations (Fig. 7(f)) was lower at Morgan's Point (0.11 m versus 0.16 m) but was marginally higher at the station closest to the entrance (0.07 m versus 0.04 m). There was no discernible difference in water level between the *fine triangular* mesh and *mixed quad-tri* mesh simulations.

Model validation statistics for total and sub-tidal velocity at the entrance current profiler are shown in Fig. 8. Differences in total velocity skill score (Fig. 8(d)) were negligible. Model skill for sub-tidal velocity (Fig. 8(h)), however, was higher for the *mixed quad-tri* mesh (0.5–0.7) while the *coarse triangular* mesh was significantly worse, particularly near the surface (skill = 0.25). There was also a clear velocity bias in the *coarse triangular* mesh simulation at the surface (Fig. 8(a) and (e)). The similar skill at

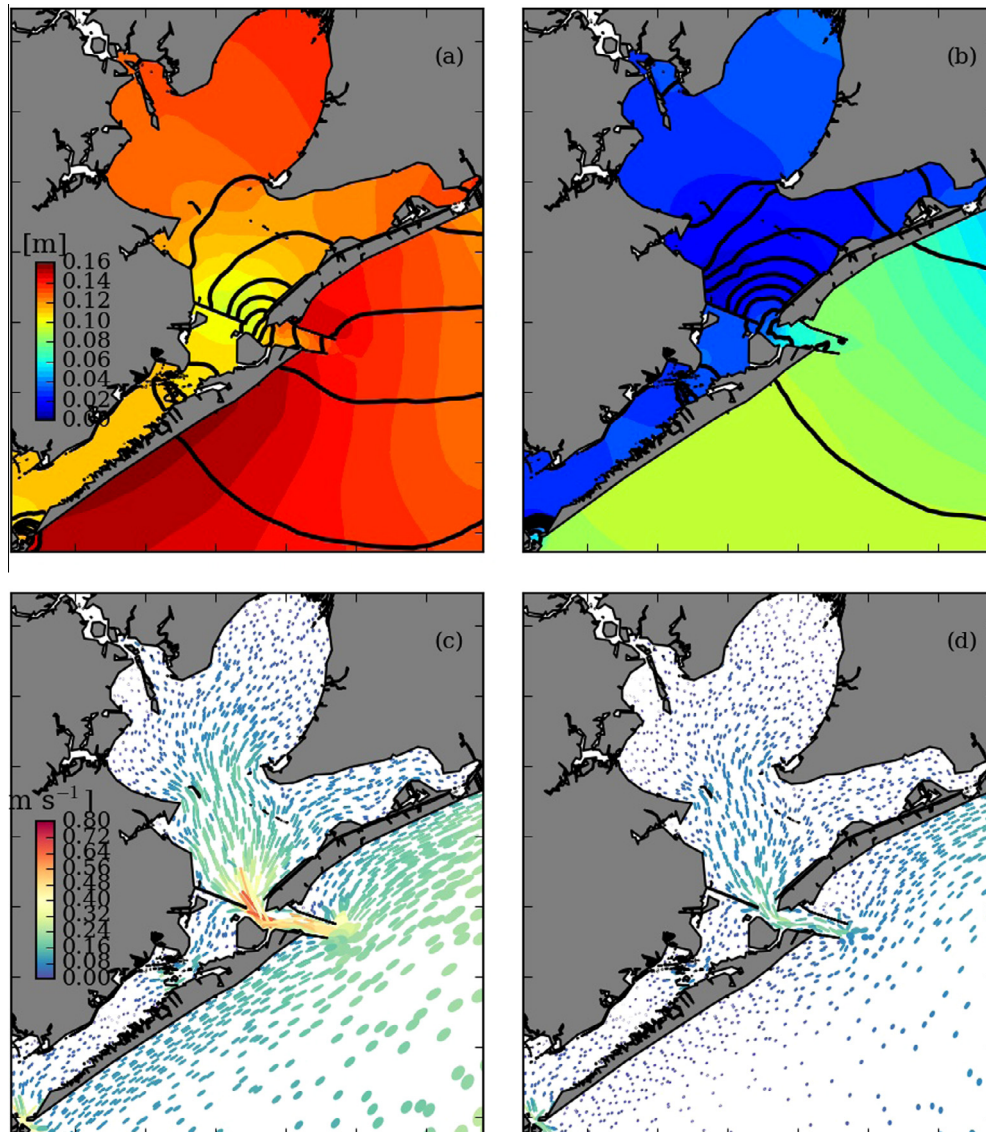


Fig. 12. Contour maps of the (a) K_1 and (b) M_2 water level tidal harmonics computed from the 2009 coarse grid scenario. Black contours indicate 0.5 h phase lines. (c) K_1 and (d) M_2 depth-averaged velocity tidal ellipses with the semi-major axis magnitude (m s^{-1}) indicated by the color. (For interpretation of the references to color in this figure legend, the reader is referred to the web version of this article.)

predicting total velocity by all three models suggests they are all capable of reproducing the tidal period variance, which dominates the sub-tidal variance. The finer meshes were better at predicting the low-frequency exchange flow at the entrance, which has important implications for transport of tracers in and out of the bay.

4.1.2. Bottom roughness sensitivity

We ran two simulations with the *mixed quad-tri* mesh, one with bed roughness of $z_0 = 2 \times 10^{-5}$ m and the other with $z_0 = 2 \times 10^{-4}$ m. Increasing the roughness decreased the positive salinity bias at the upstream sites and also decreased the salinity RMSE and improved the salinity skill score (Fig. 7(b) and (d), respectively). Modifying the roughness had a negligible effect on water level (Fig. 7(e)–(h)). Increased roughness resulted in a shift in bias in predicted currents at the entrance (Fig. 8(a)) and reduced RMSE by roughly 0.03 – 0.04 m s^{-1} (Fig. 8(b)). The total skill score was insensitive to variations in roughness while the sub-tidal velocity skill score improved with increased roughness (Fig. 8(h)).

4.1.3. Heat flux parameterization

Modeled water temperature was sensitive to the choice of heat flux parameterization (see Appendix A) and fairly insensitive to the model grid (not shown). We ran two tests: one with constant flux coefficients ($C_h = C_e = 1.1 \times 10^{-3}$), and the other with variable fluxes computed using the COARE 3.0 algorithm (Fairall and Bradley, 2003) for the entire 2011 on the *coarse triangular* grid. Results of the two experiments are plotted in Fig. 9.

Overall, all model temperature performance metrics were improved by using the COARE3.0 algorithm (Fig. 9(b)–(e)). There was a warm bias in predicted water temperature of 3 – 4 °C (Fig. 9(a) and (c)) when the Stanton, C_h , and Dalton, C_e , coefficients were set constant. The warm bias decreased by 50% in the COARE run (Fig. 9(b)).

The along-estuary water temperature gradient, estimated by the difference between the *boli* and *trin* stations, indicated that a 3 – 4 °C temperature difference developed along the length of estuary during the cooling phase of the annual cycle (see Section 2.5 and Fig. 5). In Fig. 9(b), the model replicated this gradient during the cooling period e.g., Jan–Feb 2011 and Oct–Dec 2011, with the COARE3.0 scenario performing better. However, the model predicted an opposite gradient (2 °C warmer water in Trinity Bay) during the summer period. It is unclear why this differential heating and cooling mechanism between Trinity Bay and the entrance occurred only during the cooling phase in the observations.

4.2. Spatial variability

We now will use the *mixed quad-tri* mesh simulation results to elucidate spatial details about the observed circulation presented in Section 2.

4.2.1. Tides

Observations indicated that the water level variability was distributed roughly equally between the tidal, weather system and annual frequency bands (Fig. 2). An example time series from the 2011 simulation (Fig. 10) demonstrates the ability of the model to capture the tidal (Fig. 10(a)) and sub-tidal water level variability (Fig. 10(b)).

The model reproduced the observed tidal currents throughout the water column at the entrance of Galveston Bay (Fig. 11(a)). The sub-tidal currents were also reproduced by the model (Fig. 11(b)). Strong outflows such as the event in September 2011 were captured by the model indicating that the open boundary

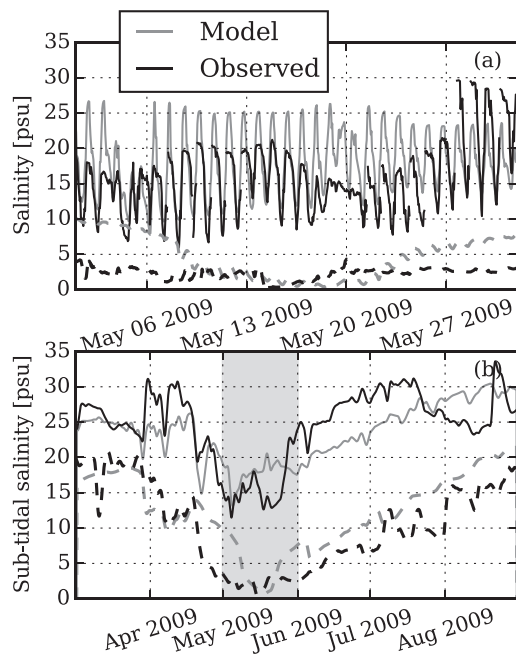


Fig. 13. Model comparison of March–September 2009 salinity at station *boli* (solid) and *trin* (dashed). (a) Raw salinity during a one-month period, and (b) sub-tidal frequency for a six-month period. Gray box in (b) indicates time-period in (a).

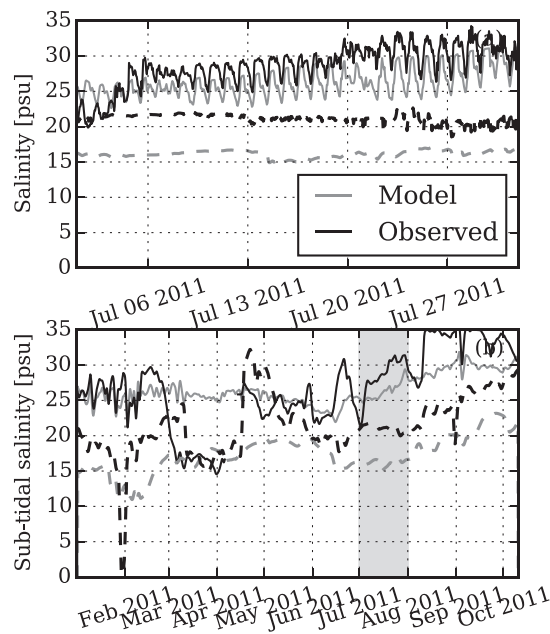


Fig. 14. Same as Fig. 13 but for 2011 model period.

and surface forcing schemes resolved the 3–10 d time scale processes.

Harmonic analysis of the modeled water level and currents indicated spatial variability of the tides consistent the observations (Section 2.2; Table 2). The amplitude of the water level oscillations at the diurnal (K_1 and O_1) and semi-diurnal (M_2) constituents were damped as they entered the bay (Fig. 12) similar to the observations (Table 2). K_1 amplitude decreased by 50% between the entrance and Texas City Dike. Trinity Bay and East Bay were tidal convergence zones where the amplitude increased again to around 80% of the entrance amplitude (Fig. 12(a)). M_2 was more rapidly damped; its amplitude decreased by 80% between the entrance

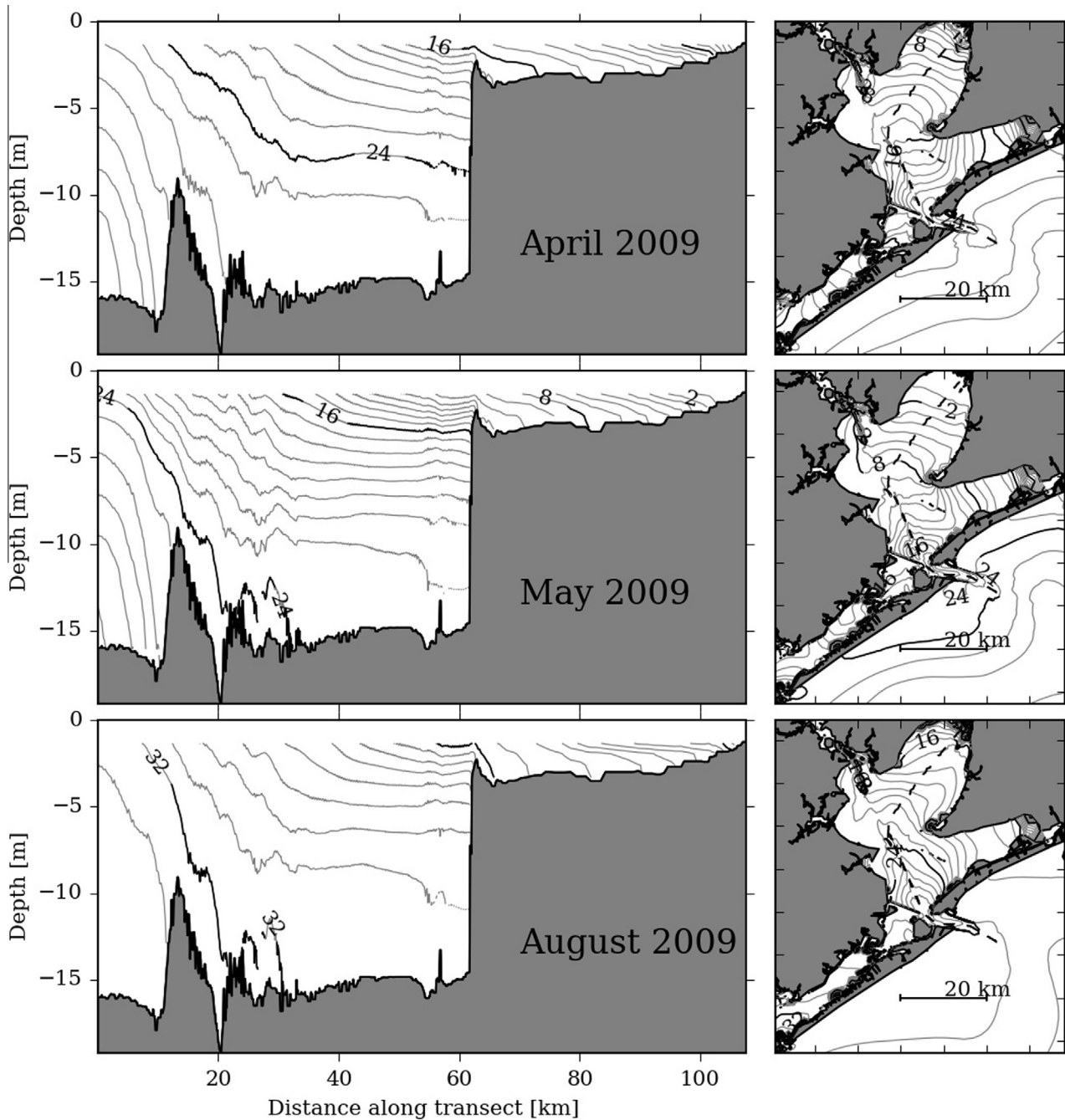


Fig. 15. Contours of modeled monthly-averaged near-surface salinity (psu) distribution in Galveston Bay using the *mixed quad-tri* grid (right column). The left column shows data along the transects indicated by the dashed line in the right column.

and Texas City Dike (Fig. 12(b)). M_2 amplitude also increased in Trinity and East Bay to roughly 40% of the entrance amplitude. A phase lag in each frequency of 5–6 h between the entrance and the upper reaches of Trinity Bay was predicted (Fig. 12). The most rapid change in phase was between the entrance channel and lower bay to Eagle Point.

The maximum magnitude of the semi-major axis of tidal ellipses of the K_1 constituent was roughly 0.8 m s^{-1} in the main entrance, around 0.2 m s^{-1} near Eagle Point and 0.05 m s^{-1} in Trinity Bay (Fig. 12(c) and (d)), a 75% to 95% reduction. The direction of the ellipses and the ellipticity (ratio of minor to major axis) were influenced by the topography. Most notably, the tidal currents were approximately rectilinear and aligned with the topography in the main inlet. Observed velocity near the entrance (see

Fig. 1) had amplitudes of 0.37 and 0.27 m s^{-1} for the K_1 and M_2 frequencies, respectively (Table 3). Model results indicated that the largest tidal ellipses (0.8 m s^{-1}) were in the center of the channel; the instrument was closer to the south bank.

4.2.2. Salinity distribution

A period of high rainfall and runoff in April 2009 freshened the entire bay between April and June (Fig. 4). The observed and predicted tidal and sub-tidal frequency salinity in Trinity Bay and the entrance is shown in Fig. 13. The *mixed quad-tri* grid model captured the trend of freshening at both stations following the flood event (see Fig. 4) and the gradual salt intrusion from June onwards. The positive salinity bias in the *mixed quad-tri* simulation (Fig. 7(a)) in Trinity Bay was evident during this intrusion period Fig. 13(b).

The model roughly predicted the tidal salinity fluctuation at both sites (Fig. 13(b)). Large amplitude salinity fluctuations of 10–15 psu at the entrance resulted from the combination of strong tidal currents, hence large horizontal excursion (see Fig. 12) large spatial salinity gradient. Sub-tidal salinity fluctuations near the entrance of roughly 5 psu were not as well reproduced. For example, during early April 2009 the salinity at the entrance (*boli*, Fig. 13(b)) shifted from 23 psu to 31 psu while the model did not predict this increase. We can only speculate that the jump was caused by high salinity coastal water advecting past the entrance that was not reproduced by the shelf ROMS model.

Observed and predicted tidal and sub-tidal salinity variability for the 2011 simulation is shown in Fig. 14. Observations indicated that low river discharge during 2011 resulted in higher than average salinity in the upper reaches of the bay with a salinity of 20–30 psu (Fig. 4). In contrast to 2009, there were no large freshening events in Trinity Bay; instead salinity increased gradually from 20 psu in January to 29 psu by October 2011. The model was initialized with a fresh bias in the upper bay and both observed and predicted salinity increased by 7–8 psu over the simulation period (Fig. 4(b)). At the entrance, salinity increased from 25–35 psu over the 2011 simulation period. The model predicted the general trend but did not capture salinity fluctuations that had a 2–4 week period.

There was an observed drop in Trinity Bay salinity during late January 2011 that was not captured in the model. In addition there were fluctuations of 10 psu in the sub-tidal salinity near the entrance (e.g., June–July 2011) that were also not captured by the model. Such events were likely due to the passage of different coastal water masses past the entrance, as previously mentioned.

Fig. 15 shows the monthly mean salinity distribution from the *mixed quad-tri* grid simulation during three different months with varying river discharge and coastal salinity. During April 2009 the salinity varied from 0 psu near the Trinity River delta to 12 psu near Eagle Point and up to 24 psu at the entrance. Following the high discharge period, the salinity at Eagle Point was 4 psu and the salinity at the entrance was 18 psu. In the period when dry conditions returned (August 2009), the salinity in Trinity Bay was greater than that before the wet period (16 psu), and the salinity at the entrance was also greater (34 psu). The ROMS model open boundary conditions (not shown) indicated that this was the result of changes in coastal circulation driving high salinity water past Bolivar Roads.

Vertical stratification, measured by top to bottom salinity difference ΔS , varied between dry and wet periods and in different parts of the bay (Fig. 15). Trinity Bay was partially stratified throughout the entire period ($\Delta S = 1$ –2 psu), while at the entrance channel ΔS was 2–4 psu. Stratification was greatest in the HSC near Eagle Point (distance = 60 km Fig. 15) and varied with river discharge; monthly-averaged ΔS was 10, 14, and 8 psu in April, May, and August, respectively.

5. Summary and conclusions

The main research goals of this study were to describe observations of circulation within Galveston Bay and to present a new three-dimensional numerical model capable of reproducing the important processes. The hydrodynamics in Galveston Bay can be summarized as follows: predominantly diurnal tides only accounted for 50% of the water level variance; the remainder of the variability was due to wind-driven coastal setup along the Texas–Louisiana shelf. Tidal currents were several times larger than the sub-tidal currents at the entrance (0.9 m s^{-1} and 0.3 m s^{-1} , respectively). Sub-tidal currents were found to be driven by wind-driven water level oscillations. Salinity variations in the bay were predominantly in response to large, intermittent

discharge events in excess of $1000 \text{ m}^3 \text{ s}^{-1}$. Salinity variations on the Texas–Louisiana shelf also drove both low and high salinity water into the bay. Water temperature oscillated with an annual cycle and a 2–3 °C horizontal gradient developed between Trinity Bay and the entrance during the cooling phase of the cycle.

Three unstructured meshes were tested to determine the role grid discretization had on predictions. In general, water level was well reproduced with all three grids, while water temperature was mainly sensitive to the surface heat flux parameterization scheme. The COARE 3.0 bulk flux algorithm significantly improved the model performance compared with using constant heat flux coefficients. Salinity and residual (sub-tidal) velocity were more sensitive to the choice of grid discretization.

During low river discharge periods (June–September 2009), the coarse grid was negatively biased (too fresh), while the *fine triangular* and *mixed quad-tri* meshes were positively biased with the *mixed quad-tri* grid being the worse performing of the two. We hypothesized that numerical diffusion was lower in the *mixed quad-tri* grid resulting in greater tidal currents and up-estuary salt flux rate that ultimately led to a higher positive salinity bias in the upper reaches of Galveston Bay. Therefore, we increased the bed roughness coefficient to compensate for the lower numerical diffusion and reduce the positive salinity bias. Increasing the grid resolution was therefore not the complete solution to a better prediction: sub-grid scale parameterizations also need to be adjusted accordingly.

The numerical model presented here has several improvements over previous Galveston Bay studies. Previous modeling efforts either made a 2D barotropic assumption (Matsumoto et al., 2005) or were 3D with a limited number (<5) of vertical layers (Berger et al., 1995; Schmalz and Grant, 2000). These models accurately reproduced the tidal frequency barotropic currents and water levels, although they were less capable at reproducing the salinity variability. Matsumoto et al. simulated a time period in 1990 with similar conditions to those in 2009, i.e. a river flooding event followed by a dry period. Because they employed relatively coarse resolution and their model was 2D, Matsumoto et al. needed to tune their model to match salinity observations by adjusting a horizontal dispersion coefficient that parameterized unresolved physical processes like tidal trapping and baroclinic circulation. Although the parameterization resulted in good agreement near the Galveston Bay mouth, the model over-predicted the salinity in Trinity Bay during the dry period. This is not surprising given that, as demonstrated in this paper, the low-frequency salinity dynamics in the upper bay are highly sensitive to model grid resolution and open boundary conditions. We demonstrated that, through use of higher horizontal and vertical resolution the SUNTANS model could accurately resolve the salinity dynamics without explicit tuning. While higher grid resolution and three-dimensionality improve predictions of the salinity dynamics in Galveston Bay, we also show that nesting with a shelf-scale model is needed to reproduce the low-frequency forcing from the Gulf. Finally, a surface heat flux model is needed to correctly reproduce the long-term effect of evaporation on the salinity.

A quantitatively validated hydrodynamic model, like the one presented here, is necessary to predict the short and long-term transport of oil and other tracers within Galveston Bay. Results presented here showed sensitivity of long-term tracer transport to grid resolution, unstructured mesh topology and choice of drag parameterization. In a future paper we will analyze salt flux mechanisms and transport time scales under different conditions.

Acknowledgments

This work was supported by a Grant from the Gulf of Mexico Research Initiative as part of the Gulf Integrated Spill Response

(GISR) Consortium. The authors gratefully acknowledge Robert Hetland for providing the ROMS model data that was used for GOM boundary conditions and the Texas Water Development Board for providing their observation dataset. We are grateful to Rusty Holleman and Steven Andrews for their assistance with the grid generation. We would like to thank two anonymous reviewers for their helpful comments on an earlier version of this article.

Appendix A. Heat flux parameterizations

We used single parameter turbulent heat flux parameterizations here that are based on a bulk flux formulation (see e.g., Kantha and Clayson, 2000). Details of the methods to compute incoming radiation can be found in e.g., Gill (1982) and Wood (2008).

Sensible heat flux (H_S): The sensible heat flux is parameterized using the following bulk formula based on the air-sea temperature gradient, the wind speed and an empirical coefficient,

$$H_S = -\rho_a c_{pa} C_h |\mathbf{U}_a| (T_w - T_a) \quad (\text{A.1})$$

where, c_{pa} is the specific heat of air ($= 1004.6 \text{ J kg}^{-1} \text{ C}^{-1}$), C_h is the Stanton number ($\approx 0.0011 - 0.0015$), T_w is the surface water temperature ($^{\circ}\text{C}$) and T_a is the air temperature at $z = 10 \text{ m}$ ($^{\circ}\text{C}$).

Latent heat flux (H_L): The latent heat flux, heat flux due to evaporation, is parameterized using the following bulk formulation,

$$H_L = -\rho_a L_v C_e |\mathbf{U}_a| (q_{sat} - q) \quad (\text{A.2})$$

where, ρ_a is the density of air (1.2 kg m^{-3}), L_v is the latent heat of vaporization ($2.5 \times 10^6 \text{ J kg}^{-1}$), C_e is the Dalton number ($\approx 0.0011 - 0.0015$), $|\mathbf{U}_a|$ is the surface wind speed [m s^{-1}], q_{sat} is the saturation vapor pressure at water surface [kg/kg] (see below), q is the specific humidity of air at $z = 10 \text{ m}$ [kg/kg] (see below). The saturation vapor pressure and specific humidity are given by,

$$q(T, P) = 0.62197 \frac{a_2}{P - 0.378a_2},$$

when $q = q_{sat}$

$$a_2 = 0.98a_1, \quad T = T_w,$$

otherwise,

$$a_2 = a_1 RH/100, \quad T = T_a,$$

where,

$$a_1 = 6.1121 \left(1.0007 + 3.46 \times 10^{-6} P \right) \exp \left(17.502 \frac{T}{T + 240.97} \right)$$

and, P is the air pressure [mb or hPa], and RH is the relative humidity [0–100%].

The dimensionless Stanton (C_h) and Dalton (C_e) coefficients are the only unknowns in these two parameterizations. Kantha and Clayson (2000) suggest a range of $1.1 \times 10^{-3} \leq C_{e(h)} \leq 1.5 \times 10^{-3}$ based on the results of many air-sea interaction experiments. We implemented two methods in SUNTANS for specifying the values to C_h and C_e . The first is simply a user-specified option where the values are manually set. The second option uses an iterative scheme proposed by Fairall et al. (1996) and Fairall and Bradley (2003) that calculates C_h and C_e as a function of wind speed as well as the air-sea temperature and humidity gradients. Grachev et al. (2011) found a reasonable agreement between the estimated sensible and latent heat fluxes using this algorithm and turbulent flux measurements taken within Galveston Bay and the Gulf of Mexico.

Upward longwave radiation ($H_{lw,u}$): The upward longwave radiation (blackbody radiation emanating from the water surface) is given by,

$$H_{lw,u} = -\varepsilon_w \sigma (T_w + T_{ref})^4 \quad (\text{A.3})$$

where, T_{ref} is the degrees Celsius to Kelvin conversion offset ($= 273.16 \text{ K}$), ε_w is the emissivity of water ($= 0.97$) and σ is the Stefan–Boltzmann constant ($= 5.67 \times 10^{-8} \text{ W m}^{-2} \text{ K}^{-4}$).

Downward longwave radiation ($H_{lw,d}$): The downward longwave radiation (blackbody radiation emanating from gases in the atmosphere) is given by,

$$H_{lw,d} = \varepsilon_a \sigma (1 - r_{lw}) (T_a + T_{ref})^4 \quad (\text{A.4})$$

where, r_{lw} is the fraction of reflected longwave radiation (≈ 0.03), ε_a is the emissivity of air

$$\varepsilon_a = \alpha_0 (1 + \alpha_{lw} C) (T_a + T_{ref})^2,$$

and $\alpha_0 = 0.937 \times 10^{-5} \text{ K}^{-2}$, α_{lw} is the cloud cover fraction coefficient ($= 0.17$), C is the variable cloud cover fraction ($\in [0, 1]$).

Shortwave radiation term (H_{sw}): The shortwave radiation source term on the LHS side of (7) has the analytical form,

$$Q_{sw}(z) = \frac{1}{\rho C_p} H_{sw} e^{-k_e z} \quad (\text{A.5})$$

where k_e is the light extinction coefficient ($= 1/L_e [\text{m}^{-1}]$; L_e is the light extinction depth). H_{sw} is the solar radiation [W m^{-2}] reaching the surface where,

$$H_{sw} = (1 - \alpha) (1 - 0.65C^2) Q_{sc}, \quad (\text{A.6})$$

and α is the surface albedo (variable, but we have used $= 0.06$). Q_{sc} is the gross incoming radiation, without clouds or reflection, given by,

$$Q_{sc} = \begin{cases} R \times S_0 \times \gamma & \gamma \geq 0 \\ 0 & \gamma < 0 \end{cases}$$

$R = 0.76$, S_0 is the solar radiation at equator ($= 1368 \text{ W m}^{-2}$), γ is an adjustment factor for time and latitude, given by

$$\gamma = \sin(\delta) \sin\left(\frac{\pi\phi}{180}\right) - \cos(\delta) \cos\left(\frac{\pi\phi}{180}\right) \cos(\omega_d t_d)$$

ϕ is the latitude [degrees], t_d is the time [year day], ω_d is the diurnal angular frequency ($= 2\pi \text{ rad d}^{-1}$) and δ is the seasonal adjustment factor, given by,

$$\delta = \frac{23.5\pi}{180} \cos(\omega_a t_d - 2.95)$$

ω_a is annual angular frequency ($= 2\pi/365.25 \text{ rad d}^{-1}$).

Appendix B. Numerical discretization of the temperature transport equation

To avoid stability limitations associated with strong vertical mixing in the presence of thin z layers, we employ the theta method (Casulli and Cattani, 1994) to discretize the vertical diffusion term in the temperature transport Eq. (7), the discrete form of which is given by

$$\frac{T^{n+1} - T^n}{\Delta t} = -A_Q^n + \theta \frac{\delta}{\delta z} \left(K_T^n \frac{\partial T^{n+1}}{\partial z} \right) + (1 - \theta) \frac{\delta}{\delta z} \left(K_T^n \frac{\partial T^n}{\partial z} \right) + \frac{\delta Q_{sw}^n}{\delta z}, \quad (\text{B.1})$$

where A_Q^n contains the advective terms discretized at time-step n , and K_T^n is at time step n to linearize the time discretization that has negligible effects on the accuracy owing to the relatively slow variability of K_T from one time step to the next. In Eq. (B.1), the shortwave radiation term is also discretized explicitly as it poses no time-step restriction for stability. Details of the discretization of the advection terms are the same as those for salt and can be

found in Chua and Fringer (2011). The discrete vertical diffusion term is given by

$$\frac{\delta}{\delta z} \left(K_T^n \frac{\partial T}{\partial z} \right)_k = \frac{1}{\Delta z_k} \left(K_{T,k+1/2} \frac{T_{k+1} - T_k}{\Delta z_{k+1/2}} - K_{T,k-1/2} \frac{T_k - T_{k-1}}{\Delta z_{k-1/2}} \right), \quad (\text{B.2})$$

where k is the index of the vertical z level and Δz_k is the height of cell k , with $\Delta z_{k\pm 1/2} = (\Delta z_k + \Delta z_{k\pm 1})/2$. At the surface, the heat flux (10) is evaluated using the surface boundary condition (8) to give

$$\frac{\delta}{\delta z} \left(K_T^n \frac{\partial T}{\partial z} \right)_{k=k_{\text{top}}} = \frac{1}{\Delta z_k} \left(Q_s(T_k) - K_{T,k-1/2} \frac{T_k - T_{k-1}}{\Delta z_{k-1/2}} \right)_{k=k_{\text{top}}}, \quad (\text{B.3})$$

where k_{top} is the index of the top cell and $Q_s(T_{k_{\text{top}}})$ implies that the terms in the heat source from (10) are a function of the surface temperature $T_{k_{\text{top}}}$. Because the theta method requires evaluation of $Q_s(T_{k_{\text{top}}})$ at time step $n+1$, an iterative solver would be needed to solve for T_k^{n+1} given the nonlinear dependence of Q_s on temperature. To avoid the iteration, the surface heat source is linearized with

$$Q_s(T_{k_{\text{top}}}^{n+1}) = Q_s(T_{k_{\text{top}}}^n) + \left(\frac{\delta Q_s}{\delta T} \right)_{T=T_{k_{\text{top}}}^n} (T_{k_{\text{top}}}^{n+1} - T_{k_{\text{top}}}^n). \quad (\text{B.4})$$

The shortwave radiation in Eq. (7) has the form

$$Q_{\text{sw}}(z) = Q_{\text{sw}0} e^{-z/L_e}, \quad (\text{B.5})$$

where L_e is the light extinction depth (m). The discrete form of the vertical gradient term in Eq. (7) was then

$$\frac{\delta Q_{\text{sw}}}{\delta z} \Big|_k = Q_{\text{sw}0} \left[\frac{\exp(z_{k+1/2}/L_e) - \exp(z_{k-1/2}/L_e)}{z_{k+1/2} - z_{k-1/2}} \right] \quad (\text{B.6})$$

Solving the shortwave penetration expression (B.6) numerically, rather than analytically, ensures that the total sum of heat prescribed into the water column matches the surface shortwave flux (Ahmed, 2013). When $d \leq L_e$ not all of the energy is accounted for by this model; some may reflect from the bottom and some may be absorbed before being re-transmitted as longwave radiation. To avoid trying to model these complex processes, we made the assumption that all of the energy is absorbed into the water column i.e., L_e was locally set to 90% of the water depth.

References

Ahmed, S., 2013. Investigations of seasonal and episodic variability in Lake Michigan currents and temperatures (Phd thesis). Purdue University.

Berger, R., McAdory, R., Martin, W., Schmidt, J., 1995. Houston–Galveston Navigation Channels, Texas Project. Tech. Rep. US Army Corp of Engineers. July.

Burchard, H., Bolding, K., Villarreal, M.R., 2004. Three-dimensional modelling of estuarine turbidity maxima in a tidal estuary. *Ocean Dyn.* 54 (2), 250–265.

Casulli, V., Cattani, E., 1994. Stability, accuracy and efficiency of a semi-implicit method for three-dimensional shallow water flow. *Comput. Math. Appl.* 27 (4), 99–112.

Chua, V.P., Fringer, O.B., 2011. Sensitivity analysis of three-dimensional salinity simulations in North San Francisco Bay using the unstructured-grid SUNTANS model. *Ocean Modell.* 39 (3–4), 332–350.

Cox, D.T., Tissot, P., Michaud, P., 2002. Water level observations and short-term predictions of Galveston Bay, Texas. *J. Waterw. Port Coast. Ocean Eng.*, 21–29 (February).

Cressie, N., 1990. The origins of kriging. *Math. Geol.* 22 (3), 239–252.

Egbert, G., Erofeeva, S., 2002. Efficient inverse modeling of barotropic ocean tides. *J. Atmos. Ocean. Technol.*, 183–204.

Fairall, C., Bradley, E., 2003. Bulk parameterization of air-sea fluxes: updates and verification for the COARE algorithm. *J. Clim.*, 571–591.

Fairall, C.W., Bradley, E.F., Rogers, D.P., Edson, J.B., Young, G.S., 1996. Bulk parameterization of air-sea fluxes for tropical ocean-global atmosphere coupled-ocean atmosphere response experiment relative analysis. *J. Geophys. Res.* 101, 3747–3764.

Fringer, O.B., Gerritsen, M., Street, R.L., 2006. An unstructured-grid, finite-volume, nonhydrostatic, parallel coastal ocean simulator. *Ocean Modell.*, 1–55.

Geyer, W.R., MacCready, P., 2014. The estuarine circulation. *Ann. Rev. Fluid Mech.* 46 (1), 175–197.

Gill, A.E., 1982. *Atmosphere–Ocean Dynamics*, vol. 30. Academic press.

Grachev, A.A., Bariteau, L., Fairall, C.W., Hare, J.E., Helmg, D., Hueber, J., Lang, E.K., 2011. Turbulent fluxes and transfer of trace gases from ship-based measurements during TexAQS 2006. *J. Geophys. Res.* 116 (D13), D13110.

Haidvogel, D., Arango, H., Budgell, W., Cornuelle, B., Curchitser, E., Di Lorenzo, E., Fennel, K., Geyer, W., Hermann, A.J., Lanerolle, L., Levin, J., McWilliams, J., Miller, A.J., Moore, A.M., Powell, T., Shchepetkin, A.F., Sherwood, C., Signell, R., Warner, J., Wilkin, J., 2008. Ocean forecasting in terrain-following coordinates: Formulation and skill assessment of the regional ocean modeling system. *J. Comput. Phys.* 227 (7), 3595–3624.

Haigh, I.D., Eliot, M., Pattiaratchi, C., 2011. Global influences of the 18.61 year nodal cycle and 8.85 year cycle of lunar perigee on high tidal levels. *J. Geophys. Res.* 116 (C6), C06025.

Hansen, D., Rattray, M., 1966. New dimensions in estuary classification. *Limnol. Oceanogr.* 11 (3), 319–326.

Hess, K., Schmalz, R.A., Zervas, C., Collier, W., 2004. Tidal Constituent and Residual Interpolation (TCARI): A New Method for the Tidal Correction of Bathymetric Data. Tech. rep., NOAA.

Hetland, R.D., DiMarco, S.F., 2012. Skill assessment of a hydrodynamic model of circulation over the Texas–Louisiana continental shelf. *Ocean Modell.* 43–44, 64–76.

Holleman, R., Fringer, O., Stacey, M., 2013. Numerical diffusion for flow aligned unstructured grids with application to estuarine modeling. *Int. J. Numer. Methods Fluids* 72 (February), 1117–1145.

Kantha, L.H., Clayson, C.A., 2000. *Small Scale Processes in Geophysical Fluid Flows*, vol. 67. Academic Press.

Klinck, J., Hofmann, E., 2002. Impact of channelization on oyster production: a hydrodynamic–oyster population model for Galveston Bay. *Texas Environ. Modell. Assess.*, 273–289.

Lester, L.J., Gonzalez, L.A., 2011. The State of the Bay: A Characterization of the Galveston Bay Ecosystem. Tech. rep., Texas Commission on Environmental Quality, Galveston Bay Estuary Program, Houston.

Marta-Almeida, M., Hetland, R.D., Zhang, X., 2013. Evaluation of model nesting performance on the Texas–Louisiana continental shelf. *J. Geophys. Res. Oceans* 118 (5), 2476–2491.

Matsumoto, J., Powell, G.L., Brock, D.A., 2005. Effects of Structures and Practices on the Circulation and Salinity Patterns of Galveston Bay, Texas. Tech. Rep., Texas Water Development Board, February.

Mellor, G., Yamada, T., 1982. Development of a turbulence closure model for geophysical fluid problems. *Rev. Geophys.* 20 (4), 851–875.

Mesinger, F., DiMego, G., Kalnay, E., Mitchell, K., Shafran, P.C., Ebisuzaki, W., Jović, D., Woollen, J., Rogers, E., Berbery, E.H., Ek, M.B., Fan, Y., Grumbine, R., Higgins, W., Li, H., Lin, Y., Manikin, G., Parrish, D., Shi, W., 2006. North American regional reanalysis. *Bull. Am. Meteorol. Soc.* 87 (3), 343–360.

Murphy, A., 1988. Skill scores based on the mean square error and their relationships to the correlation coefficient. *Mon. Weather Rev.*

Orlando, S., 1993. Salinity characteristics of Gulf of Mexico estuaries. Tech. rep., NOAA.

Powell, E.N., Klinck, J.M., Hofmann, E.E., McManus, M.A., 2003. Influence of water allocation and freshwater inflow on oyster production: a hydrodynamic–oyster population model for Galveston Bay, Texas, USA. *Environ. Manag.* 31 (1), 100–21.

Reed, M., Johansen, O.I., Brandvik, P.J., Daling, P., Lewis, A., Fiocco, R., Mackay, D., Prentki, R., 1999. Oil spill modeling towards the close of the 20th century: overview of the state of the art. *Spill Sci. Technol. Bull.* 5 (1), 3–16.

Schmalz, R., 2000. Three-dimensional hydrodynamic model developments for a Galveston Bay nowcast/forecast system. Tech. Rep., NOAA, November.

Schmalz, R., Grant, T., 2000. High-resolution Houston ship channel ADCP and CTD survey: model-data intercomparisons. Tech. Rep. NOAA Technical Report NOS CS 6, March.

Schoenbaechler, C., Guthrie, C.G., 2012. Coastal Hydrology for the Trinity–San Jacinto Estuary. Tech. rep. Texas Water Development Board, Austin, Texas.

Schroeder, W.W., Wiseman, W.J., 1999. *Geology and hydrodynamics of Gulf of Mexico estuaries. Biogeochemistry of Gulf of Mexico Estuaries*. Wiley, 3–22.

Taylor, L., 2008. Digital Elevation Model of Galveston, Texas: Procedures, Data Sources, and Analysis. Tech. rep. National Geophysical Data Center.

Thomson, R.E., Emery, W.J., 2001. *Data Analysis Methods in Physical Oceanography*. Elsevier.

Wang, B., Giddings, S.N., Fringer, O.B., Gross, E.S., Fong, D.A., Monismith, S.G., 2011. Modeling and understanding turbulent mixing in a macrotidal salt wedge estuary. *J. Geophys. Res.* 116 (C2), C02036.

Wolfram, P.J., Fringer, O.B., 2013. Mitigating horizontal divergence checker-board oscillations on unstructured triangular C-grids for nonlinear hydrostatic and nonhydrostatic flows. *Ocean Modell.* 69, 64–78.

Wood, T.M., 2008. Modeling Hydrodynamics and Heat Transport in Upper Klamath Lake, Oregon, and Implications for Water Quality Scientific Investigations. Tech. rep. United States Geological Survey.

Zhang, X., Hetland, R.D., Marta-Almeida, M., DiMarco, S.F., 2012. A numerical investigation of the Mississippi and Atchafalaya freshwater transport, filling and flushing times on the Texas–Louisiana Shelf. *J. Geophys. Res.* 117 (C11), C11009.